Charles University
Faculty of Science
Institute of Geochemistry, Mineralogy and Mineral Resources

Study programme: Geology
Branch of study: Geochemistry

Bc. Anna Shevchenko

Assessment of the effect of clay minerals on biomarker detection in evaporites using Raman spectrometry

Posouzení vlivu přítomnosti jílových minerálů na detekci biomarkerů v evaporitech pomocí Ramanovy spektroskopie

Master's thesis

Thesis supervisor: Mgr. Adam Culka, Ph.D.

Prague, 2024

Declaration of Authorship

I hereby declare that this diploma thesis is my own original work and has not been submitted for any degree or professional qualification at any other university or institution. I confirm that all sources used and cited have been indicated and acknowledged by means of complete references.

In Prague, 24.07.2024 .....

Bc. Anna Shevchenko

Acknowledgements

First and foremost, I would like to express my deepest gratitude to my supervisor, Mgr. Adam Culka, Ph.D., for invaluable guidance, support throughout the course of my research and perfoming pXRF analyses of clay mineral samples. I am also thankful to RNDr. Irena Matulková, Ph.D. from the Department of Inorganic Chemistry, Faculty of Science, for the access to the hydraulic press Trystom H-62 and her kind assistance and to doc. Mgr. Petr Drahota, Ph.D. from our institute for conducting the X-ray diffraction analyses of clay mineral samples.

Abstract

This thesis investigates the detection limits of biomarker β-carotene in experimentally prepared evaporite – clay mineral matrices using a miniaturized handheld Raman spectrometer RaPort. Miniaturized Raman spectrometers are analytical instruments of growing importance for astrobiological rover missions on Mars. Rovers are equipped with a variety of tools to detect biosignatures — evidence of past microbial life — possibly embedded in evaporite minerals, which are considered potential preservers of organic compounds. However, Martian surface mineralogy poses a challenge. Laser-induced fluorescence from clay minerals can overwhelm weaker Raman signals, thus complicating the detection of biomarkers. Given the likelihood of clay minerals coexisting with evaporites on Mars, we tried to understand how this combination affects detection limits of biomarker β-carotene using this miniaturized Raman spectrometer. In this study, we prepared mixtures with varying weight percentages of two distinct clay minerals in gypsum. We analyzed these mixtures at different concentrations of β-carotene, which was chosen to be a referential biosignature molecule for the experiment. Our findings revealed specific patterns and trends in the spectral behavior of these mixtures. As well as some variations in the spectral interference caused by differences among various types of clay minerals.

Keywords: Raman spectrometry, miniaturized Raman spectrometer, astrobiology, Mars, biosignatures, clay minerals, evaporites, β-carotene

Abstrakt

Tato diplomová práce se věnuje vyhodnocení detekčních limitů β-karotenu, jako biomarkeru, v experimentálně připravených matricích evaporitu ($CaSO_4 \cdot H_2O$) a vybraných jílových minerálech za použití miniaturizovaného ručního Ramanovského spektrometru RaPort. Miniaturizované Ramanovské spektrometry jsou analytické nástroje rostoucího významu v astrobiologii, jsou důležitou součástí analytického vybavení roverů hledajících stopy života na Marsu. Rovery jsou vybaveny různými nástroji k detekci potenciálních biosignatur – známek minulého mikrobiálního života – které mohou být zachovány v evaporitech, jež jsou považovány za vhodné geologické prostředí pro vznik, a především zachování organických sloučenin. Avšak mineralogie povrchu Marsu je komplikovaná, a polohy evaporitických minerálů přímo sousedí s polohami jílových minerálů. Navíc, některé navržené techniky počítají s odběrem a homogenizací vzorků těchto hornin před samotnou Ramanovskou analýzou. Laserem indukovaná fluorescence jílových minerálů tak může překrývat slabší Ramanovský signál, což by mohlo komplikovat detekci biomarkerů. Vzhledem k pravděpodobnosti koexistence jílů s evapority na Marsu, jsme se snažili pochopit, jak tato kombinace ovlivňí detekční limity β-karotenu jako biomarkeru za použití miniaturizovaného Ramanovského spektrometru. V této studii jsme připravili směsi s různými podíly dvou odlišných jílových minerálů v sádrovci. Analyzovali jsme směsi při různých koncentracích β-karotenu, který byl vybrán jako referenční biosignaturní molekula pro tento experiment. Naše zjištění odhalila specifické trendy ve spektrálním chování těchto směsí, stejně jako i některé spektrální variace způsobené různými typy jílových minerálů.

Klíčová slova: Ramanova spektroskopie, miniaturizovaný Ramanovský spektrometr, astrobiologie, Mars, biomarkery, jílové minerály, evapority, β-karoten

Table of Contents

1. Introduction

1.1. Object of research

The object of research for this thesis is to evaluate the impact of fluorescence from clay minerals on detectability of biomarkers in evaporites using miniaturized Raman spectrometer. This study is particularly relevant in the context of exobiology and Martian exploration. Currently, Mars rovers like NASA's Perseverance, and the upcoming ExoMars rover mission, are equipped or will be equipped with compact Raman spectrometers to analyze the Martian surface for signs of past life. However, Mars presents a unique challenge due to its mixed mineralogy, where evaporites and clay minerals often coexist. Evaporites can potentially encapsulate the remnants of primitive organisms, serving as biomarkers. However, the fluorescence emitted by clay minerals can overshadow the weaker Raman signal from organic compounds, complicating their detection.

1.2. Aims and objectives

The aim of this research is rooted in the quest to uncover signs of past life on Mars, a primary objective of contemporary planetary exploration missions. By investigating how fluorescence from various clay minerals impacts on detection of biomarkers, we can refine our interpretation of data from Mars missions and develop better strategies for identifying biosignatures. We hope that insights gained from this study can provide valuable guidance for the development of future instruments and exploration techniques. The aim of this study is to simulate such conditions to understand the limitations and capabilities of compact Raman spectrometers in detecting biomarker signals amidst fluorescent interference from clay minerals. This involves testing clay minerals with different weight percentages (wt%) and varying concentrations of biomarker. We hope to gain a clearer understanding of the current technological capabilities and limitations in identifying potential biosignatures on Mars.

In summary, our aim is to bridge the gap in our current knowledge regarding the interference of clay mineral fluorescence in Raman detection of biomarkers. By doing so, we contribute to the broader goal of enhancing the scientific tools used in the search for extraterrestrial life, particularly in the challenging environment of Mars.

2. Evaporites and biomarkers

2.1. Organics and biomarkers

In a historical context, views within the scientific community concerning the definition of the term *biomarker* (especially in astrobiology) gradually evolved. And ultimately, nowadays the term 'biomarker' became more narrowly specified. According to Brocks (2011), biosignatures or biomarkers – are molecular remnants of lipids or other natural substances. In sedimentary environments, lipids that escape the remineralization process are typically chemically reduced to hydrocarbon skeletons. Encased within sedimentary rocks, these skeletons can remain preserved for hundreds of millions of years. The structure of biomarkers is often closely related to their original precursors and can be indicative of specific groups of organisms.

It's important to highlight that not all carbon-based substances or molecules are biomarkers. Several examples of organic compounds can be found in extraterrestrial environments, which aren't obligate derivatives of biochemical processes. I would like to mention some of them.

Carbonaceous chondrites, primitive stony meteorites, preserve a record of chemical evolution spanning 4.5 billion years. Biggest part of the carbon in these meteorites is organic, primarily presented as hydrocarbons. For example, the amino acid composition of Murchison meteorite has been explored in detail. Over 70 amino acids have been confirmed in hot-water extracts, including 8 protein amino acids and 11 others commonly found in biological systems (Cronin et al., 1995). Amino acids in meteorites do not necessarily possess a biological origin, as their formation can occur through abiotic processes including chemical reactions and radiation-induced transformations in extraterrestrial environment. Another organic-rich carbonaceous chondrite has been investigated, the Allende meteorite. The organic founds in this meteorite include a variety of compounds such as hydrocarbons, aldehydes and PAHs (Zenobi et al., 1989).

During pyrolysis of Martian sedimentary material using SAM (Sample Analysis at Mars) various chlorinated hydrocarbons, such as chloromethane, chloromethylpropene, chlorobenzene etc. were detected above background levels (Glavin et. al., 2013). However, later laboratory studies indicated that heating samples containing oxychlorines, such as chlorates (ClO_3^-) and perchlorates (ClO_4^-), along with organics present on the surface of Mars, can produce chlorinated hydrocarbons (Millan et. al., 2020). Authors named PAHs, amino and carboxylic acids as potential source organics on the Martian surface). However, it is important to reiterate that these chemical compounds are not biosignatures.

To better understand the potential for life on Mars, studying terrestrial analog sites can provide valuable insights. Foucher et al., 2021 describe and classify by their function different type of analogue sites on Earth, which can be used for astrobiology purposes. Exploring of ones can be used for determination of

specific cellular requirements needed in such environments, potentially occurring on other planetary bodies. That can help us to find perfect understanding of biomarkers. Studying extremophiles and their biochemical adaptational mechanisms also can expand our understanding (Kochhar et al., 2022).

The example of salterns may serve as a good illustration. Salterns, which are hypersaline environments used for salt production all over the world, are home to a variety of microorganisms. Halophilic microorganisms must regulate their osmotic balance to survive in such conditions and there are two adaptation strategies for this. First one involves accumulating inorganic salts, primarily potassium chloride (KCl), inside the cell to balance the osmotic pressure ("salt-in" strategy). The other one is accumulating organic solutes in the cytoplasm for the same purpose ("compatible-solute" strategy). Storing KCl in the cytoplasm requires much less energy and is advantageous for energy-limited microorganisms.

The "salt-in" strategy is employed by two phylogenetically distinct groups: the aerobic, extremely halophilic archaea of the order *Halobacteriales* and the anaerobic, halophilic bacteria of the order *Haloanaerobiales*. However, in cells employing this strategy for osmotic adaptation, all enzymes and structural elements must be suited to high salt concentrations to ensure the proper functioning of the intracellular enzymatic systems. In the majority of other halophilic microorganisms, osmotic balance is achieved through small organic molecules that the cells either synthesize or absorb from surrounding environment (Oren, 1999; Vítek, 2010). "Compatible-solute" strategy doesn't require specially adapted proteins. Compatible solutes are defined as molecules that, even at high concentrations, permit efficient enzymatic functions. Compatible solutes found in halophilic microorganisms include polyols, sugars and sugar derivates, amino acids and their derivatives, and quaternary amines

Microorganisms employ specific strategies to survive in environments with intense UV radiation. One key adaptation involves producing organic compounds that absorb UV light, effectively shielding against its harmful effects. These compounds act as a passive defence mechanism by absorbing UV radiation before it can damage cellular components. Additionally, microorganisms have evolved mechanisms to manage reactive oxygen species (ROS) and repair UV-induced damage, particularly to DNA (Cockell and Knowland, 1999).

One of such compounds is scytonemin, which is a specialized UV-screening pigment synthesized by certain cyanobacteria, notably by those inhabiting extreme environments exposed to intense UV radiation, such as desert crusts and hot springs. It's a yellow-brown, water-insoluble pigment composed of indole-alkaloid derivatives and amino acids. Scytonemin exhibits significant screening ability, attenuating light by 2 to 55% at 320 nm at the single-cell level. When cells are situated beneath layers of microbial mats or within cell colonies, this screening effect can be even more pronounced, particularly against UV-A radiation (Garcia-Pichel and Castenholz, 1993).

Another large group of photoprotective compounds are carotenoids. Certain carotenoids with shorter chains have the potential to function as UV-screening pigments, carotenoids that are widely distributed and contain 9 or more conjugated double bonds primarily absorb light in the visible spectrum, especially in the blue range of irradiation. β-carotene is produced in large quantities by halo-tolerant microalgae *Dunaliella salina* (Xi et. al., 2020) and acts as both a protective pigment and an antioxidant against ROS (Pourkarimi et. al., 2020).

Within the framework of this diploma thesis a representative of carotenoid pigments β-carotene will be considered as a model biomarker. This group of biomolecules was selected based on their unique features described before. This protection allows microorganisms to survive and thrive in environments exposed to high levels of solar radiation.

One of β-carotene functions is protection against oxidative stress. Carotenoids act as an antioxidant, collecting bigger part of reactive oxygen species (ROS) generated under stressful conditions such as high UV radiation, high temperature, high salinity or exposure to toxic compounds. ROS can damage cellular components like proteins, lipids, and DNA, leading to cell death or dysfunction. By neutralizing ROS, carotenoids help extremophiles with maintaining cellular integrity and functionality in harsh environments. β-carotene can modulate gene expression in response to environmental stressors as high salinity, helping microorganisms with adaptation to changing conditions (Giani and Martínez-Espinosa, 2020). It may influence the expression of genes involved in stress response pathways, DNA repair mechanisms, and metabolic processes, enabling microorganisms to survive and even thrive in extreme environments.

Chemically β-carotene is a highly conjugated hydrocarbon and a member of the carotenoid family. Carotenoids are a large family of naturally occurring pigments found in plants, algae, fungi, bacteria, and some animals. They are characterized by their long-conjugated double-bond systems, which give them their distinctive colors ranging from yellow to red. Carotenoids are tetraterpenoids, meaning they are composed of 8 isoprene units (C_5H_8). This gives them a general molecular formula of $C_{40}H_{56}$. They have a polyene chain (a series of alternating single and double bonds) that can be capped with cyclic end group. The conjugated double-bond system of carotenoids absorbs light in the visible region (400-500 nm), resulting in colors ranging from yellow to red. The exact absorption maxima depend on the length and structure of the conjugated system.

Carotene exists primarily in three forms: α, β, and γ. The key distinction lies in their conjugated double bonds: for example, α-carotene possesses 10 conjugated double bonds, whereas β-carotene has 11.

Besides β-carotene there are various carotenoids produced by archaea. For example, bacterioruberin (Fig. 1). It is a C50 carotenoid pigment produced by certain halophilic archaea, such as *Halobacterium salinarum*. Bacterioruberin is located in cell membrane and acts as an antioxidant, neutralizing ROS,

and contributes to membrane stability and fluidity, is known for its bright pinkish-red color. Carotenoids are so brightly colored as they have an allowed π- π* molecular transition in visible spectrum, with their color shifting from yellow to red as the number of conjugated double bonds increases. For example, β-carotene has 11 conjugated double bonds and is orange, while bacterioruberin has 13 and is red. (Marshall et al., 2007).

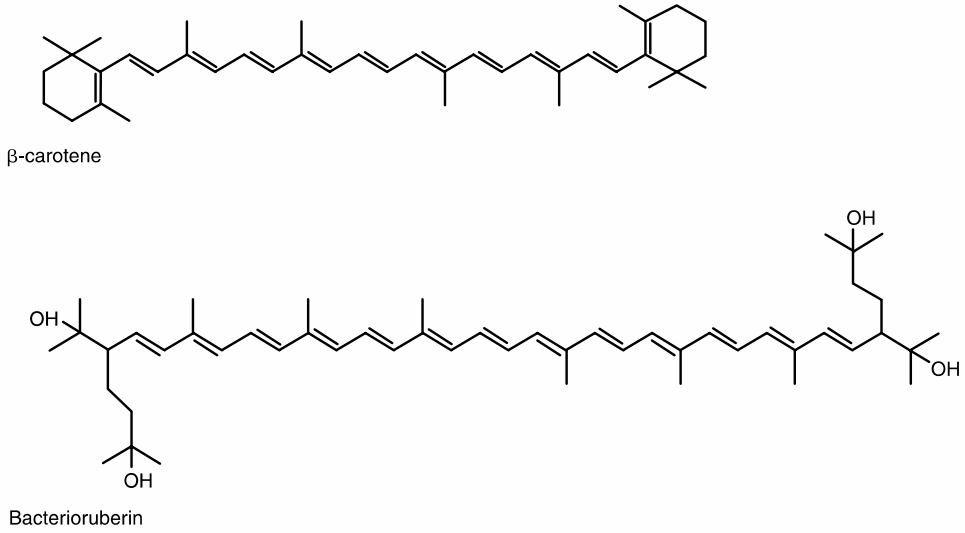

Fig. 1. Comparation of molecular structure of carotenoids: β-carotene and bacterioruberin

At the same time, while described environmental conditions may be viewed as excellent analogs for exobiological purposes, also as described microbiological adaptation strategies, it doesn't automatically imply that life emerged and inhabited similar locations elsewhere in the solar system. Despite this, our research will be based on the hypothesis that possible extraterrestrial life developed in a similar way, and colonization of environments followed the same patterns as on Earth.

2.2. Preservation of biomarkers

Evaporites, sedimentary rocks formed by the precipitation of minerals from evaporating water, provide a unique protective habitat for microorganisms. These environments can include halite, gypsum, anhydrite, and other minerals, which crystallize as bodies of water like lakes and seas dry up. The extreme conditions associated with evaporite formations might seem inhospitable, yet they create refuges that can support microbial life.

Within evaporite deposits, microorganisms can form biofilms or microbial mats. These complex communities consist of various microbial species that interact synergistically. The biofilms create microenvironments with gradients of nutrients and waste products, facilitating the survival and growth of diverse microbial populations (Gunde-Cimerman et. al., 2018). There is an example of hypersaline

mat from La Salada de Chiprana, Spain reported by Prieto-Barajas et al., 2018, where mat have developed under condition with concentration of magnesium 7x higher that of seawater.

A significant subset of microorganisms found in evaporites are endolithic microorganisms, which live inside the rock matrix. Endoliths inhabit the tiny pore spaces, providing them with a stable environment that buffers against external temperature extremes and desiccation. The rock itself offers a physical barrier to UV radiation and protects these microorganisms from other environmental stresses (Wierzchos et al., 2006). Endolithic microorganisms are often found in extreme environments on Earth, such as deserts, polar regions or deep-sea hydrothermal vents. These environments may resemble conditions found on other celestial bodies, such as Mars or moons like Europa and Enceladus.

Oren et. al., 1995 describe layered microbial community thriving within a gypsum crust at the bottom of a hypersaline saltern pond in Eilat, Israel, with salinity ranging from 280 to 290 g/L. Optical analysis using fiber-optic microprobes revealed that the upper crust of gypsum absorbs blue light due to protective carotenoids, while red and infrared light penetrate deeper, supporting photosynthesis at varying depths within the crust.

Interestingly, in the early 90s the model of endolithic microorganisms in salt crystals on Mars was mentioned by Rothschild, 1990. Within evaporites, endolithic organisms inhabit microenvironments that shield them from external hazards like intense UV radiation and extreme temperature fluctuations. Also, endolithes are often well-preserved within evaporites, offering opportunities to study ancient microbial communities and their organic residues. The metabolic activities of endolithic microorganisms can leave behind distinct organic remnants in their host rocks. Detecting these signatures in rocks from other planetary bodies could provide evidence for past or present life and guide future astrobiological exploration missions.

For example, in salterns, the concentration of salt increases as water evaporates, leading to the formation of evaporites. As the brine becomes more concentrated, microorganisms and their metabolic products, including β-carotene, can become trapped within the forming salt crystals. As crystals form, they can encapsulate microorganisms or organic particles suspended in the brine. This process effectively traps β-carotene within the salt matrix. Later it can persist in evaporites through a combination of factors related to its chemical stability, the protective properties of the matrix in which it is embedded, and the environmental conditions of the evaporites (Stivaletta et. al., 2010). β-carotene is a hydrophobic molecule, making it less susceptible to hydrolytic degradation in aqueous environments. This property helps it remain stable in evaporitic conditions, where water activity is limited.

Evaporites often trap and preserve microorganisms or their biosignatures within their mineral matrices. These preserved compounds provide valuable insights into ancient microbial ecosystems and their survival strategies under extreme conditions. Low permeability and a stable chemical environment that

shields them from external chemical changes and radiation are ideal conditions for the long-term preservation of microorganisms.

For example, Schubert et. al., 2010 describe ancient *Dunaliella* cells co-trapped with prokaryote cells inside salt core from Death Valley, USA. Authors report about orange and green coloration that can indicate the presence of intact pigment molecules such as chlorophyll and carotenoids. Interestingly, but β-carotene released from the cell showed no signs of degradation, despite sensitivity of pigment to light and oxygen. 34,000 years of incorporation inside halite crystal obviously was in low-oxygen condition with lack of sunlight. Also, ancient halite brine inclusion from Death Valley was described by Winters et. al., 2013. Carotenoids there were detected by Raman spectroscopy, producing characteristic Raman bands at 1000–1020 cm^{-1} (v_3), 1150–1170 cm^{-1} (v_2), and 1500–1550 cm^{-1} (v_1), when exposed to visible laser excitation. Presence of characteristic carotenoid bands was repeated at various depths, indicating stability of these organic molecules. More recent report is from Chaka Salt Lake, Western China, where carotenoids were detected via Raman spectroscopy in the solid phase of fluid inclusions (Chen et. al., 2021).

In conclusion, it can be inferred that study of microorganisms in different evaporites on Earth has significant implications for astrobiology, particularly in the search for life on Mars and other planetary bodies.

2.3. Evaporites

Evaporites are minerals that form through the evaporation of water, typically in arid environments where evaporation exceeds precipitation. These minerals precipitate from saline waters and are commonly found in sedimentary deposits. Evaporites are commonly found in natural environments like salt flats, saline lakes, desert playa lakes and so on. Already mentioned salterns or salt pounds, where seawater or brine is evaporated to harvest salt is a good example of human-made sites with various evaporitic minerals. These ponds are designed to maximize evaporation for producing halite and other commercially valuable evaporites.

The formation of evaporite deposits involves a sequence of stages where minerals precipitate from an evaporating water body by stages due to their varying solubility. These stages occur as the concentration of dissolved ions increases, eventually reaching supersaturation and precipitating specific minerals (Copeland, 1967).

The sequence of crystallization is shown on Fig. 2 and follows a predictable order based on the solubility of various minerals as the water evaporates and becomes more concentrated. Initially, as the evaporation process begins, carbonates such as calcite ($CaCO_3$) and aragonite are the first to precipitate. These minerals have relatively low solubility. Evaporation continues and the concentration of dissolved ions

increases, leading to the precipitation of sulfate minerals. Gypsum ($CaSO_4 \cdot 2H_2O$) is typically the next to form. Following the sulphates, halide minerals like halite (NaCl) start to precipitate. In the later stages of evaporation, as the brine becomes extremely concentrated, potassium and magnesium salts begin to crystallize. Sylvite (KCl) and carnallite ($MgKCl_3 \cdot 6H_2O$) are typical minerals that form during this stage. In the final stages, the remaining brine is highly concentrated, leading to the precipitation of late-stage and minor minerals. These include polyhalite ($K_2Ca_2Mg(SO_4)_4 \cdot 2H_2O$) and bischofite ($MgCl_2 \cdot 6H_2O$), among others (Warren, 2006).

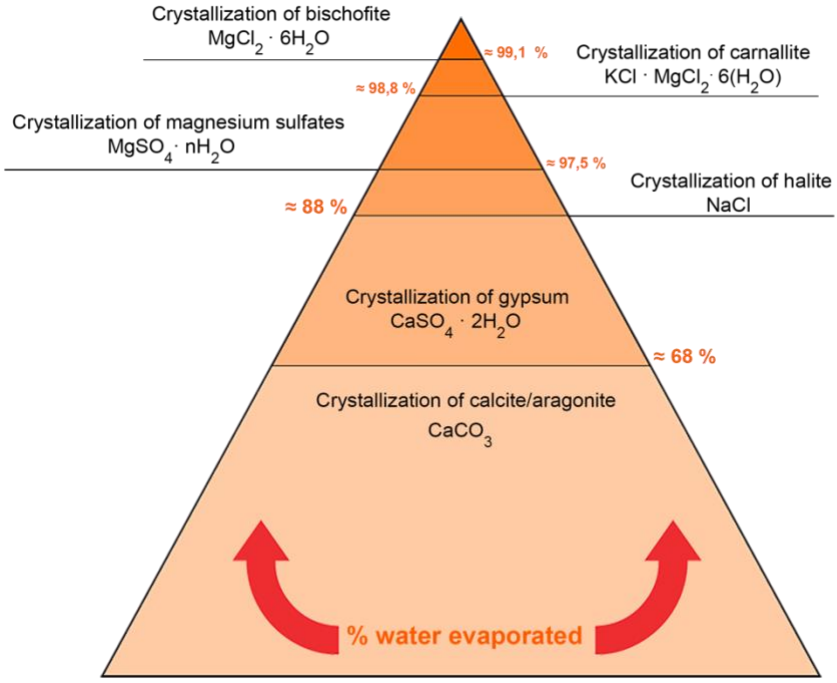

Fig. 2. Sequence of crystallization of evaporites

The study of evaporites from the point of view of astrobiology and planetary geology is very important, their presence on Earth and other planetary bodies, like Mars, provides strong evidence of historical environments where liquid water once existed and then evaporated, leaving behind mineral deposits. Evaporite minerals can trap and preserve organic molecules and microfossils, potentially providing evidence of past microbial life. In the following text sulphates and their distribution on Mars will be analysed in detail.

It is also notable that terrestrial S/Cl ratio is lower compared to Martian. The sulphur to chlorine ratio on Earth and Mars reflects their distinct geochemical environments, driven by differing geological and atmospheric processes (Clark and Baird, 1979). On Earth, the S/Cl ratio is lower, due to the dominance of chloride ions from abundant NaCl. In contrast, Mars has a significantly higher S/Cl ratio, as its surface is rich in sulphates like epsomite, gypsum and jarosite.

2.4. Sulphates on Mars

Sulphates present on Mars play a significant role in unraveling the planet's geological history. Their presence often indicates the past presence of water, as many sulphate minerals form through processes involving aqueous alteration or the evaporation of water-rich solutions. Therefore, investigating sulphates can provide valuable insights also into the hydrological cycle, climate dynamics, and potential habitability. Additionally, understanding the geological context of sulphates helps in interpreting the stratigraphy, depositional environments, and alteration processes that have formed Martian surface.

First data on sulphur enrichment and correlation between sulphur and magnesium was received from X-ray fluorescence analysis during Viking mission (Clark et al., 1982). Later, during the Mars Pathfinder mission similar data was obtained from the APXS (Alpha Particle X-ray Spectrometer) for soil and rock samples, confirming sulphur enrichment and its correlation with magnesium. Enrichment in Br, Cl and Cr also was detected. This suggested that some of the magnesium existed in the form of magnesium sulphate (Rieder et. al., 1997, Haskin et al., 2005). Additional data from the APXS analysis of the subsurface dust suggested that the primary component was Mg-sulphates, with smaller amounts of Ca-sulphates and possibly Fe-sulphates as jarosite - $KFe_3(SO_4)_2(OH)_6$ (Wang et. al., 2006). Interestingly, Fe^{3+} presence was also confirmed by Mössbauer spectrometry data.

Jarosite precipitates under oxic and acidic conditions where pH < 4. It forms in environment rich in sulphate ions and iron, typically where water interacts with iron-bearing minerals. Martian basaltic lithology consists primarily of volcanic rocks formed from the solidification of magma. These basalts are rich in iron and magnesium and typically contain minerals such as olivine or pyroxene. The weathering of these basaltic rocks under acidic and oxidizing conditions can lead to the formation of secondary minerals like jarosite.

Later in 2003 European Space Agency's (ESA) launched Mars Express spacecraft equiped with OMEGA (Observatoire pour la Minéralogie, l'Eau, les Glaces et l'Activité) spectrometer. During the mission characteristic NIR spectral peaks of sulphates were also observed (Bibring et. al., 2005). OMEGA spectral data was later processed and mapped in detail by Gendrin et. al., 2005. By analyzing the OMEGA dataset, specific combinations of absorption band characteristics, such as central position and shape, were identified. Data was compared to calibration spectra obtained from terrestrial analogues, allowing to classify three spectral types associated with sulphates (Fig. 3).

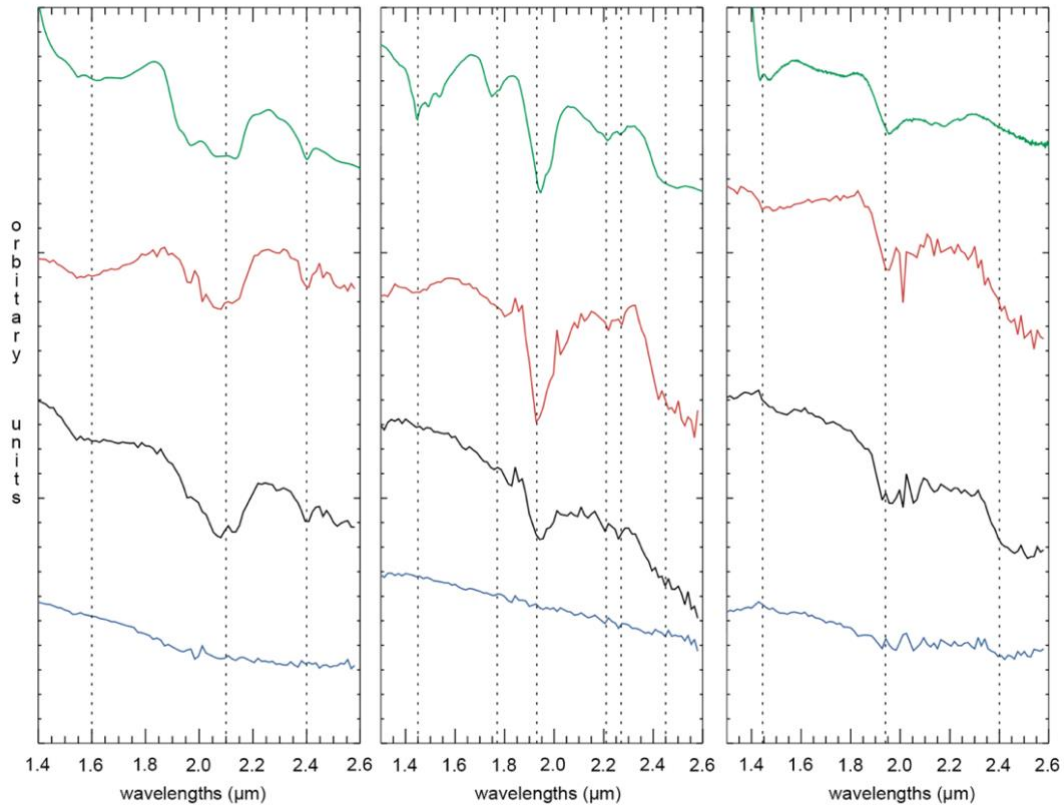

Fig. 3. Comparation of obtained spectra by Gendrin et. al., 2005. Green coloured: library spectrum, black: the OMEGA spectrum, blue: reference spectrum, and red: the spectral ratio. There are spectra for kieserite (left), gypsum (centre), and polyhydrated sulfate (right).

In summary, three spectral models for sulphates were presented by authors. The first spectral type displays absorptions at 1.6, 2.1, and 2.4 μm. In hydrated conditions, the notable 2.4 μm band arises from the $(SO_4)^{2-}$ stretch, indicating monohydrated sulphates. Kieserite ($MgSO_4 \cdot H_2O$), a type of magnesium monohydrated sulphate, closely aligns with the OMEGA spectrum. The second spectral type exhibits five absorption bands at wavelengths of 1.4, 1.75, 1.9, 2.2, and 2.4 μm. Absorption bands at 1.4 and 1.9 μm indicates hydrated mineral. 1.4 and 2.2 μm bands consist of smaller ones and have double shape. Authors describe these features as indicative for Ca-sulphates such as gypsum ($CaSO_4 \cdot 2H_2O$) or bassanite ($2CaSO_4 \cdot H_2O$). Third spectral type also can be characterized as indicative hydrated mineral with 1.4 and 1.9 μm absorption bands. Specific feature at 2.4 μm arises from the $(SO_4)^{2-}$ stretch in a hydrated environment. It manifests plateau-like asymmetrical shapes, which indicate polyhydrated sulphates. According to authors, sulphates with various cations closely match the OMEGA spectrum, epsomite ($MgSO_4 \cdot 7H_2O$) was chosen as best fitting.

Data about evaporites from Mars Exploration Rover was analysed by Tosca et. al., 2005. Their geochemical modelling suggests that acidic fluids from weathered olivine-rich basalt supposed to be enriched in Mg, Fe, SO_4 and slighter in Ca. The weathering results in the formation of Mg, Ca, and Fe-

sulphates like jarosite and melanterite - $FeSO_4 \cdot 7(H_2O)$. This working theory thus confirms some of the data obtained earlier.

Later evidence of sulphate deposites was described from Northeast Syrtis, the site which failed in the competition with Jezero crater during designing of the Mars 2020 rover mission. Quinn and Ehlmann, 2019 describe deposition of sulphates, exposed at northeast Syrtis Major forming a 600-meter-thick sequence that underwent deposition, alteration, and erosion. Siliciclastic sediments, enriched in polyhydrated sulphates, were deposited on slopes and thinned against older Noachian highlands. According to authors, these layered sulphates experienced fracturing during diagenesis.

Crisler et. al., 2012 experimented with halotolerant bacteria from Great Salt Plains (Oklahoma, USA) and its ability to grow in condition of high concentration of magnesium sulphate, specifically in 2 M solutions of epsomite. Among the bacterial isolates tested, 35% were capable of growth under these conditions. The bacteria exhibited complex physiological responses when exposed to mixtures of $MgSO_4$ and NaCl, along with other environmental stressors. Growth was also observed at 1 M concentrations of various sulphate salts. The study illustrates that certain terrestrial microorganisms capable of thriving in highly saline environments may adapt to conditions resembling those found on the surface of Mars.

Another similar study focuses on the Spotted Lake (British Columbia, Canada). It's a hypersaline lake exhibiting SO_4^{2-} concentrations around 271 g/L and 51,4 mg/L for Mg^{2+}. Through metagenomic sequencing of Spotted Lake sediments, was characterized microbial community dominated by bacteria, particularly Proteobacteria, Firmicutes, and Bacteroidetes (Pontefract et. al., 2017).

3. Clay minerals

3.1. Characteristic of clay minerals

Term *clay mineral* refers to significant group of hydrous aluminum silicates characterized by a layered, sheet-like structure and extremely small particle size. These minerals can include significant amount of iron, alkali or alkaline earths metals. Clay minerals are formed through the weathering and alteration of pre-existing rocks, especially those rich in minerals like feldspar and mica (Encyclopædia Britannica). As a result, clay minerals are often found in sedimentary rocks, soils, and other weathered materials. They are characterized by their unique crystal structure, which consists of layers of interconnected silica tetrahedra and alumina octahedra. That's why main classification of clay minerals is based on their layer structure.

Clay minerals are usually defined as <4 μm particles, in some categorization even <2 μm (Huggett, 2013). This is the reason, why they cannot be easily characterized using standard optical or physical methods. Crystallography and structure of clays was understood better only with the advent of XRD technique in the first half of the 20th century.

An understanding of the evolution of clay minerals through different alteration processes is crucial for gaining insight into the mineralogical history of Earth and other celestial bodies. And even though clay minerals were not present during the initial high-temperature phases of planetary formation, they have become a significant element in the near-surface crustal environments of Earth, Mars, and the celestial bodies as carbonaceous chondrite meteorites (Hazen et al., 2013).

3.2. Physical properties and structure

As already mentioned, there is a commonly used classification of clay minerals. They are classified into two categories based on the way how tetrahedral and octahedral sheets are arranged within layers. There is 1:1 (T-O – tetrahedral-octahedral) and 2:1 (T-O-T – tetrahedral-octahedral-tetrahedral) group. Schematic representation is shown on Fig. 4.

Every single layer of 1:1 clays is constructed from a tetrahedral (SiO_4) and an octahedral sheet (AlO_6). The layers are held together by sharing oxygen atoms at their interfaces. It results a relatively simple and compact crystal structure. Kaolinite is a common mineral in this group. The basic formula for a 1:1 clay can be represented as $Al_2Si_2O_5(OH)_4$, where Al is in the octahedral and Si is in the tetrahedral sheet (Kumari and Mohan, 2021). The actual mineral composition may vary. Cation exchange capacity of clays in this category is relatively low.

In the 2:1 group the mineral structure consists of two tetrahedral layers sandwiched between one octahedral layer. The presence of interlayer spaces allows easy exchange of cations and makes isomorphous substitutions quite typical. Isomorphic substitution involves the replacement of specific atoms or ions within the crystal structure without changing the overall structure. Silicon in the tetrahedral sheet may be replaced by aluminum through isomorphic substitution. This substitution is common and contributes to the overall negative charge of the clay mineral. In the octahedral sheet aluminum may be replaced by magnesium or other cations (Guggenheim et al., 1997). In addition there is classification into expanding subgroup such as smectites and non-expanding subgroup as illite. Expansion occurs during moisture absorption.

Sometimes a separate third 2:1:1 group of clays is defined. It comprises two silica tetrahedral and one aluminum octahedral layer, with a magnesium hydroxide sheet occupying the interlayer space between the 2:1 sheets. The 2:1:1 group is primarily represented by chlorite, characterized as iron-magnesium silicates with some aluminum atoms.

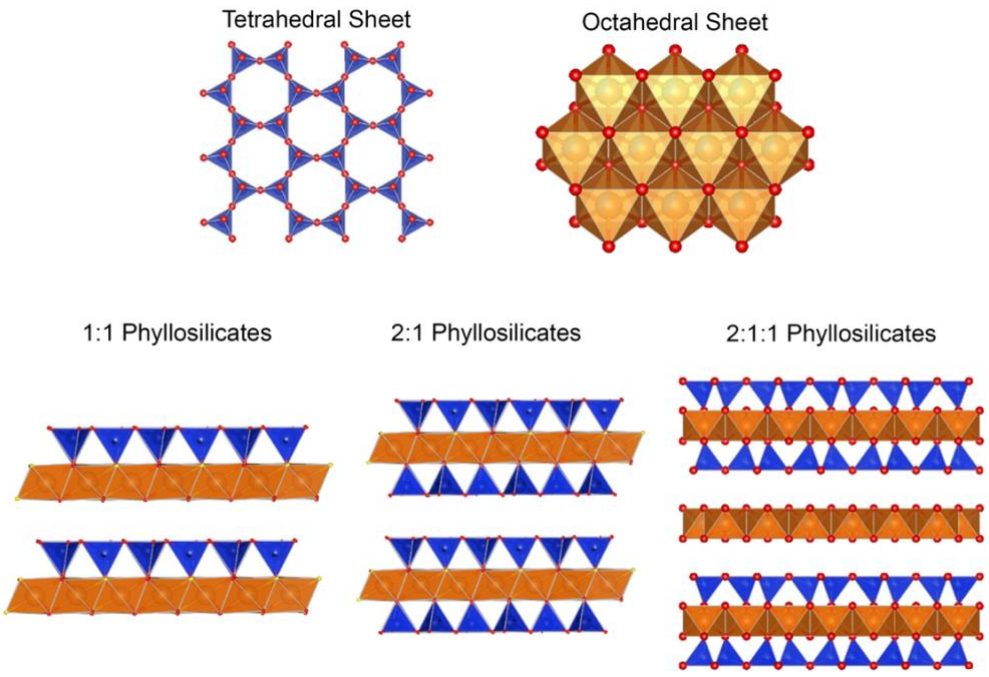

Fig. 4. Arangement of different types of clay minerals (Pavón and Alba, 2021)

Summarizing information about clay minerals we can define certain significant characteristics. According to Bergaya and Lagaly, 2006 there is an anisotropic layered arrangement, presence of various surface types (external basal, edge surfaces, interlayer surfaces). Thereto it's an ability to be easily modified by processes such as adsorption or ion exchange. Plasticity, high specific surface area and incorporation external substances (organic compounds and large molecules) through intercalation – these characteristics can also be mentioned.

3.3. Clays on Mars

Presence of phyllosilicates on the surface of Mars offers insights into the ongoing and historical weathering processes that have taken place on the planet. That's why, for more than twenty years, the scientific exploration on Mars has focused on investigating clay minerals, which are significant indicators of past water activity on the planet. The identification of clays on Mars can be traced back to the 1980s, when different absorption spectra were observed in Earth-based telescopes.

The majority of information regarding mineral typology and distribution on Mars was obtained through the utilization of two primary methods. These methods can be categorized into remote and direct techniques. Remote or indirect methods are based on analyzing data from a distance using instruments like spectrometers or telescopes. Direct methods rely on studying material directly on the Martian surface using various instruments carried by rovers and landers. Both remote and direct approaches contribute to our understanding of Martian mineralogy.

In 2003 European Space Agency's (ESA) launched Mars Express spacecraft with the primary objective of studying the geology, mineralogy and atmosphere of Mars. The spacecraft was equiped with OMEGA (Observatoire pour la Minéralogie, l'Eau, les Glaces et l'Activité) spectrometer. This instrument allows to identify spectral fingerprints of different minerals including clays. The ones were initially identified in some significant rock formations located in the southern highlands. Presence of Fe-rich and Mg-rich smectites was detected over Noachian outcrop in Syrtis Major by analyzing NIR spectra (Poulet et al., 2005).

Spectral analysis derived from MRO Compact Reconnaissance Imaging Spectrometer for Mars (CRISM) outputs has similar results. Fe-rich phyllosilicate (such as nontronite) were the most commonly detected, although sometimes Al-rich clays were locally dominant (Wray et al., 2009). On several sites Fe/Mg clays were covered by Al-rich phyllosilicates. One of the observations of this specific transition was made in the Nili Fossae region by CRISM. On this site kaolinite-bearing layer is situated on top of the thicker formation composed of Fe/Mg smectites (Ehlmann et al., 2009). Subsequently, other studies have also reported similar stratigraphy of these minerals in other Martian regions. As stated in Bishop et al., 2008 there are two distinct assemblages of phyllosilicates in Mawrth Vallis: underlying Fe/Mg smectites and overlying Al-bearing clays with hydrated silica. According to later study of Mawrth Vallis, kaolinite, allophane and montmorillonite spectrally dominanted in uppermost Al-rich layer (Bishop and Rampe, 2016).

Mawrth Vallis, Nili Fossae and Valles Marineris sites are quite specific and represent layered phyllosilicates phenomena, which also was recognized in separated location such as Eridania basin (Noe Dobroe et. al., 2008). That’s why, there is an assumption that similarly layered clays could be

widespread. Exposed formations in Mawrth Vallis are characterized by distinct polygonal texture and noticeable layer separation (Fig. 5). Layer of Fe/Mg-rich clay forms the lowermost level, covered by stratum consisting of Al-rich clay possibly montmorillonite or hydrated silica (Mustard et. al., 2008). There are some hypothesis of layered clays origin: alteration of volcanic ash, hydrothermal alteration, marine sedimentation, pedogenesis and other. In any case, it can be concluded that there is a range of variations not only in chemistry of clays, but also in their possible stratigraphic configuration.

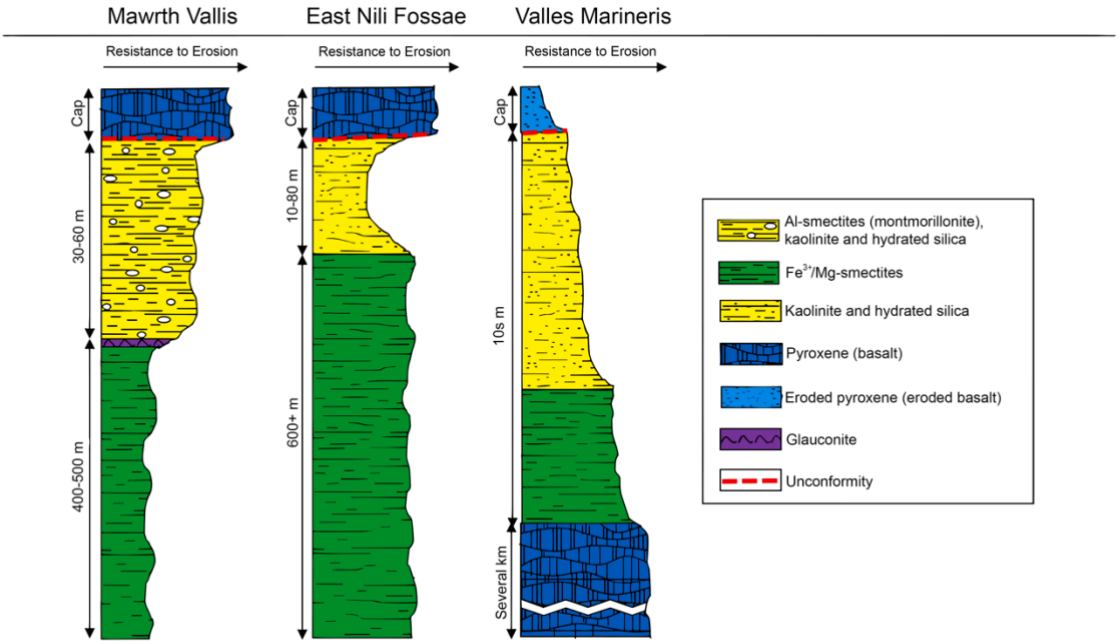

Fig. 5. Stratigraphy of clay deposits on several sites on Mars (modified from Gainey, 2022)

It's worth mentioning that there are interpretations of relative ages of some sediment classes, due to stratigraphy based on spectral data. The interpretation shown on Fig. 6 was originally proposed by Bibring et al., 2006 and was based on data from OMEGA**.** According to authors there was a sequence of 3 eras in Martian history. *Phyllosian* (characterized by nonacidic aqueous alteration, traced by phyllosilicates), later *theiikian* (acidic aqueous alteration indicated by sulphates) and last one – *siderikian* (anhydrous, traced by ferric oxides). Climate change event between two first eras is characterized as a transition from an alkaline and likely moist environment to an acidic, possibly driven by surface volcanic activity. Authors also highlight that potentially habitable conditions could have formed during the phyllosian era, because clays could have functioned as specific habitats for the essential biochemical activities.

Later the model was supplemented with newer data derived from Mars Reconnaissance Orbiter. Murchie et. al., 2009 define several distinct classes of aqueous mineral-bearing deposits including phyllosilicates, clay-sulphates, carbonate and gypsum deposits within the Bibring's model. Several of them should be studied in more detail.

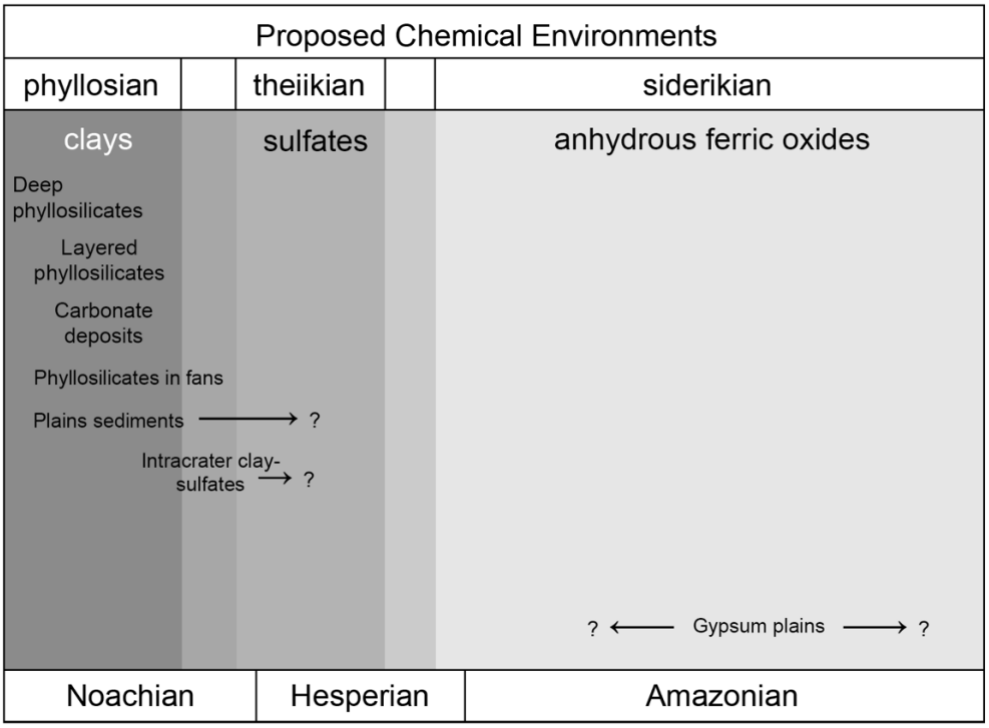

Short Name	Aqueous Minerals Present	Morphology	Distribution
Layered phyllosilicate	Al smectite, kaolinite group, Fe/Mg smectite, hydrated silica, Fe oxides	10s-m thick blanket of Al phyllosilicate and hydrated silica overlying Fe/Mg smectite, commonly polygonally fractured; exposed where protective caprock has been removed	Mawrth Valles and surrounding regions, Nili Fossae; small exposures elsewhere
Phyllosilicates in intracrater fans	Fe/Mg smectites from drainage basins	Fan-shaped deposit where channel debouches into crater; phyllosilicate typically in lower, tabular strata	Holden, Eberswalde, Jezero, Terby craters
Plains sediments	Chlorides and Fe/Mg smectites	Eroded remnants of phyllosilicate-rich deposits in topographic low, sometimes forming piedmont; may be embayed by chloride	Scattered throughout highland plains in crater floors and intercrater plains
Deep phyllosilicates	Various phyllosilicates, dominated by prehnite, chlorite, Fe/Mg smectite	Massive or bouldery to layered outcrops in crater walls and central peaks, massifs, and chasma walls and escarpments	Craters walls and central peaks in highland plains, walls of Valles Marineris

Fig. 6. Model of chemical environments on Mars (modified from Murchie et. al., 2009)

Deep phyllosilicates and layered phyllosilicates classes are described as the oldest ones from phyllosian era and Fe-Mg smectites are common in both categories. In the case of layered phyllosilicates Fe/Mg smectites may alternate with Al-rich ones and kaolin group clays.

Phyllosilicates in intracrater fans are described as the next one deposit class and are typical for fan-shaped sites, where channels flow into basins. Delta-like deposits and alluvial fans at the end of channels suggest the transport and deposition of material by flowing water. These channels can take on different forms, including braided channels, dendritic networks, or even small, narrow gullies. Such a class could

potentially represent Jezero crater site, which is a chosen site for Perseverance rover mission. Fe/Mg smectites are described as a key aqueous mineral. These phyllosilicates are spectrally similar to those found in different parts of the drainage basins. Typically, they're situated in the lower planar parts of the fans, which is characterized by absence of distinct blocks, indicating the presence of fine-grained materials deposited in a calm environment.

These smectites are also typical for the plains sediments class, where chlorides also occur. As a conclusion, we can indicate that Fe–Mg-rich smectitic clay minerals are the most common clays on the Martian surfaces considered by this spectral model.

It is important to highlight that remote sensing equipment installed on spacecrafts can provide valuable global context, however, this approach may not have the ability to perform the detailed analysis. The way to resolve this problem is developing advanced *in situ* methods.

Rover is a type of robotic vehicle designed to move across the surface of planet, to perform scientific exploration, analyses and data collection. The Soviet Union attempted Mars exploration missions in the early 1970s, including Mars 2 and Mars 3 rovers. Both of them were unsuccessful. The first rover was destroyed during the landing, while with Mars 3 communication was lost 110 seconds after landing.

The first wheeled vehicle to roam on Mars successfully was the Sojourner rover. Sojourner was a small, solar-powered rover with six wheels landed on Mars on July 4, 1997. It was designed primarily to study and test technical aspects of such *in situ* expedition. Matijevic, 1997 describes, „Primary mission of experiment is to determine microrover performance in the poorly understood planetary terrain of Mars". Secondary goal for rover was studying nearby rock formations at the landing site – Ares Vallis in Chryse Planitia. The chemical analyses conducted by the Sojourner have been recast into possible minerals on site. In NSSDC's report, 1997 is indicated the presence of orthopyroxene, feldspars, quartz, and additional minerals such as magnetite, iron sulfide and calcium phosphate. In summary, there was no data presented about the presence of clays on the Martian surface from this mission. Nevertheless, Sojourner demonstrated the workability of rovers for planetary exploration and paved the way for more advanced rover missions.

In 2004 the rover Opportunity landed on Mars in Meridiani Planum. In comparison to earlier missions, Opportunity was equipped with a more advanced set of scientific instruments: it included wide-angle navigation camera, spectrometers, and rock abrasion tools. The landing site was chosen based on the data obtained from the Mars Global Surveyor TES (Thermal Emission Spectrometer) beforehand. Christensen et al., 2000 mentioned higher concentrations of hematite in rock formations in Meridiani Planum (15-20% by fractional area). Hematite can form through various mechanisms, several of them are driven by liquid water. Layered bedrock formation was already captured in the first photo taken by

onboard rover camera. Later, Opportunity rover explored other formations where similar layered features were discovered, including small-scale ripple cross-lamination (Squyres et al., 2004).

It is worth considering that there are also examples when spectral data did not ultimately match the data obtained during the rover mission. The Mars Reconnaissance Orbiter (CRISM) detected phyllosilicates on Cape York site - specifically in the form of smectite. In the early 2010s Opportunity examined terrain to verify this spectral observation. Farrand et al., 2013 analyzed multispectral observations of Cape York made by rover. However, spectral data were compared with library spectra of Fe/Mg smectites (nontronite, hectorite, and saponite) and results showed no similarity.

Moving in chronological order, in 2012 Mars Science Laboratory (MSL) – next NASA's mission landed on Mars and began exploring the planet's surface. One of the mission's primary goals was exploration for habitable environments and investigation the mineralogy of Mars, including phyllosilicates detection. The rover, named Curiosity explored several locations, such as the Yellowknife Bay area of Gale Crater. Rover made several noteworthy discoveries regarding clay minerals on Mars. John Klein and Cumberland are two specific locations within the Yellowknife Bay formation that were investigated by the Curiosity rover during its mission. According to Vaniman et al., 2014 analysis of samples from John Klein and Cumberland sites, diffraction band maximum is indicative of a trioctahedral clay mineral such as saponite or Fe – saponite. Authors conclude that clays in John Klein are trioctahedral, likely saponitic smectites.

Ehlmann and Edwards, 2014 summarize essential findings in mineralogy of Mars from both orbiting and landed missions (Fig. 7). Compilation was made for data received since the Mars Global Surveyor Mission in 1997.

Class	Group/mineral/phase	Formula
Phyllosilicates (clay minerals)	Fe/Mg smectites (e.g., nontronite, saponite)	$(Ca, Na)_{0.3\text{-}0.5}(Fe, Mg, Al)_{2\text{-}3}(Al, Si)_4O_{10}(OH)_2 \cdot nH_2O$
	Al smectites (e.g., montmorillonite, beidellite)	$(Na, Ca)_{0.3\text{-}0.5}(Al, Mg)_2(Al, Si)_4O_{10}(OH)_2 \cdot nH_2O$
	Kaolin group (e.g., kaolinite, halloysite)	$Al_2Si_2O_5(OH)_4$
	Chlorite	$(Mg, Fe^{2+})_5Al(Si_3Al)O_{10}(OH)_8$
	Serpentine	$(Mg, Fe)_3Si_2O_5(OH)_4$
	High-charge Al/K phyllosilicates (e.g., muscovite, illite)	$(K,H_3O)(Al,Mg,Fe)_2Al_xSi_{4-x}O_{10}(OH)_2$

Fig. 7. Compilated mineralogical data on clay minerals (modified from Ehlmann and Edwards, 2014)

Next significant step in the exploration of Mars was The Perseverance rover mission, officially known as NASA's Mars 2020. It builds on the successes of earlier investigation of Mars made by rovers, such

as Sojourner, Spirit, Opportunity, and Curiosity. There were several objectives named as primary for Perseverance: studying planet's past habitability, searching for signs of ancient microbial life on Mars and sample collection. For these purposes, the rover was equipped with advanced technical equipment such as SHERLOC (Scanning Habitable Environments with Raman and Luminescence for Organics and Chemicals), PIXL (Planetary Instrument for X-ray Lithochemistry), sustainable power source that uses a radioisotope thermoelectric generator and other techniques.

Site for Perseverance rover exploring also wasn't chosen randomly, it was based on theory that Jezero crater once was a lake. There are several features pointing to this: crater's shape, structure, and prominent river delta, resulting from the transportation and deposition of sediment by water over a significant period. These features such as delta-like deposits or alluvial fans, can indicate that material was transported and deposited by flowing water. These specific landforms typically form when a fluid carrying sediment slows down and deposits the sediment as it enters a larger body of water or spreads out. According to above mentioned analysis of combined spectral data from CRISM, OMEGA and Thermal Emission Spectrometer, phyllosilicates are widespread near and inside Jezero crater. Present on site aqueous minerals are described as iron/magnesium smectites from drainage basins.

Summarizing all data obtained and analysed using spectral observations and rover missions on Martian surface we can offer a conclusion. The main goal of that data compilation is to determine the most relevant types of clays, which can be used in the practical part of this diploma thesis. Priority is to select widespread, representative, and accessible mineral(s) for our simulation. According to data compilation, Fe/Mg smectites are mostly dominant on Martian surface. Next groups of phyllosilicates in terms of prevalence are Al smectites and kaolin group clays.

4. Raman spectroscopy as an analytical tool

4.1. Principles and instrumentation of Raman spectroscopy

In 1928, Indian physicist Sir C. V. Raman, along with his colleague K.S. Krishnan, discovered the Raman effect by observing that when light traverses a transparent material (they used several very pure liquid organic compounds), a small fraction of the light that is scattered has different wavelengths than the incident light. This phenomenon, which results from inelastic scattering of photons by molecules, leads to a shift in the light's wavelength.

It is worth to mention that on May 6, 1928, G. Landsberg and L. Mandelstam from the USSR submitted a paper to Die Naturwissenschaften titled "Eineneue Erscheinung bei der Lichtzerstreuung in Krystallen" (A new phenomenon in light scattering by crystals), which was published on July 13, 1928. This paper detailed their observation of frequency changes when monochromatic light was scattered by quartz. Soviet physicists observed inelastic scattering of light and discovered the same scattering phenomenon around the same time as their Indian colleagues (Long, 1988). Raman and Krishnan's work was published slightly before Soviet one and quickly gained widespread acclaim. In 1930 Raman received the Nobel Prize in Physics.

Huge theoretical contribution that preceded the experimental discoveries was made in 1923 by Austrian physicist Adolf Smekal, which predicted the phenomenon of inelastic scattering of light.

From a quantum theory perspective, Raman effect genesis involves the interaction between photons and the quantized vibrational modes of molecules within a sample. Radiation of frequency v can be viewed as a stream of photons with energy hv, where h is Planck's constant. When these photons interact with molecules, they are scattered. In the case of elastic scattering (Rayleigh), photons will be emitted from their original direction without changing their energy. A monochromatic photon from a laser source interacts with a molecule in the sample. However, upon interaction, the photon's energy can be also absorbed by the molecule, exciting it from ground vibrational state to a virtual energy state. In the virtual state, molecule exists before relaxing back to a different vibrational state. During relaxation, the molecule emits a photon with energy different from that of the incident photon (Fig. 8).

During this process, molecule can either gain or lose some of its energy, according to the rules of quantization: energy is changed by an ΔE value, which corresponds to the difference in energy between two of its quantum states. If the molecule gains energy ΔE, the scattered photon will have an energy of $hv - \Delta E$ and a corresponding frequency of $v - \Delta E/h$. Conversely, if the molecule loses energy ΔE, the scattered photon will have a frequency of $v + \Delta E/h$. Scattered radiation with a frequency lower than incident is called Stokes, while radiation scattered at a higher frequency is known as anti-Stokes (Бенуэлл, 1985).

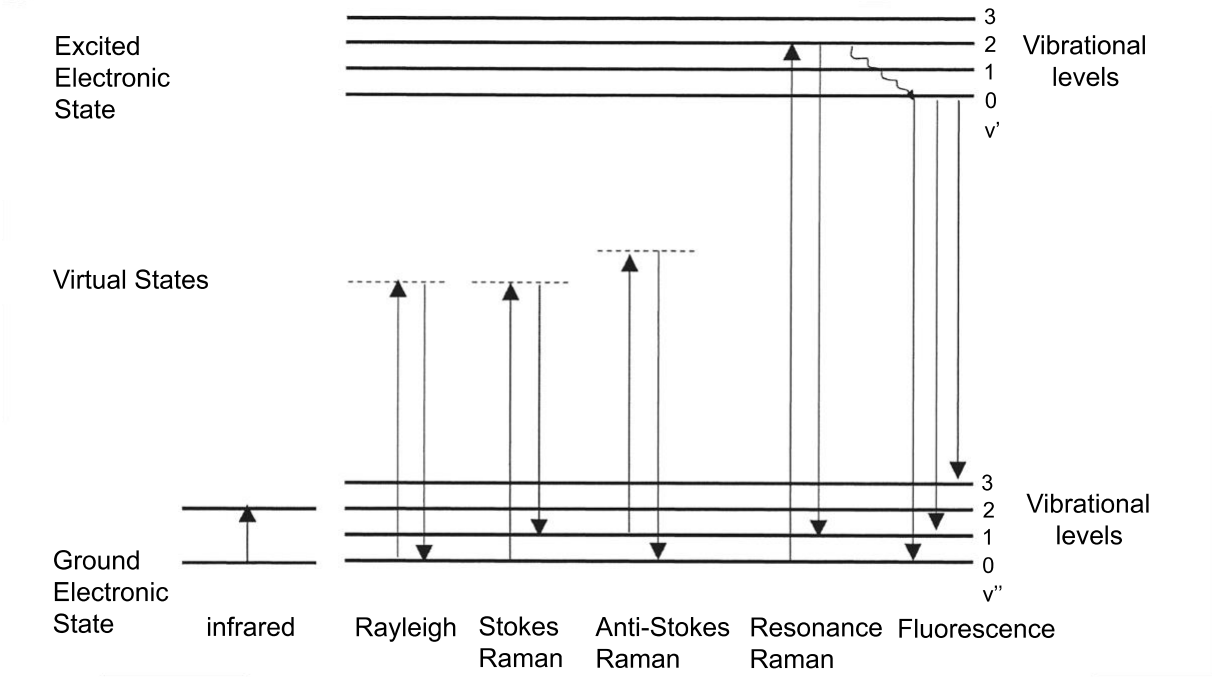

Fig. 8. Schematic demonstration of different types of scattering (Marshall 2007, modified Carey 1982)

Stokes and anti-Stokes scattering are fundamental processes in Raman spectroscopy, describing how photons interact with molecules and providing us with valuable information about their vibrational energy levels. Stokes scattering, as already mentioned, occurs when a molecule absorbs energy from an incident photon and emits a photon with less energy (longer wavelength) than the incident one. On the other hand, Anti-Stokes scattering occurs when a molecule loses energy during its vibrational relaxation process. The molecule relaxes to a lower-energy vibrational state by emitting a photon with higher energy (shorter wavelength) than the incident one.

Measurements are typically expressed in units of reciprocal centimeters (cm^{-1}). This unit represents the wavenumber of the scattered light, which is directly related to the energy of the molecular vibrations. When a sample is analyzed using a Raman spectrometer, the instrument detects the shifts in frequency (wavenumber) of the scattered light compared to the incident laser light. These shifts correspond to the vibrational modes of the molecules in the sample. Vibrational modes describe specific patterns of oscillation or vibration of atoms or molecules within a material. These modes include stretching, bending, torsional, and lattice vibrations. Each mode (of a specific molecule) has a characteristic frequency or energy associated with it, which can be analyzed using spectroscopic techniques.

The development of Raman instrumentation has a rich history. Early Raman spectrometers were relatively rudimentary, utilizing mercury lamps as light sources and photographic plates to record spectra. The weak intensity of light sources and the low sensitivity of detectors meant that obtaining spectra could take hours or even days. Researchers used colored filters and chemical solutions to isolate

specific wavelength ranges, but these early instruments were limited by the dominance of Rayleigh scattering, which obscured weaker Raman signals (Long, 1977).

The invention of Raman laser in 1962 by G. Eckhardt and E.J. Woodbury marked a turning point for the analytical Raman spectrometry (Eckhardt et. al., 1962).

The introduction of fiber Raman lasers, which used optical fibers as the Raman medium happened during the 1980s. Optical fibers offered numerous advantages, including flexibility, compactness, and the ability to transmit light over long distances with minimal loss.

Later, in the 2000s and 2010s advancements in the miniaturization and portability of Raman spectroscopy devices were made. There was a shift from bulky, laboratory-based instruments to compact, handheld, and portable devices that brought Raman spectroscopy to a wider range of applications and environments. Portable Raman spectrometers enabled *in situ* analysis in various environments, provided with immediate results. In addition, many portable devices featured user-friendly interfaces, making them accessible to non-experts also. Miniaturisation enabled conducting sophisticated analyses in remote and extreme environments, such as those found on other planets and moons, portable spectrometers have been integrated into the payloads of planetary rovers.

4.2. Organic compounds detection

Wavenumber area of Raman spectrum can be roughly divided into 3 main regions: fingerprint, silent and CH / OH stretching region. In addition to the vibrations of specific functional groups, the Raman spectrum can also reveal vibrations of the molecular scaffolding, known as skeletal vibrations. These vibrations are usually found below 1500 cm^{-1} in the fingerprint region.

The fingerprint region is generally ranging from 300 to 1900 cm^{-1} and includes a multitude of peaks that arise from the complex vibrational interactions within a molecule, including both functional groups and the overall molecular skeletal vibrations (Anton Paar Wiki). This part of Raman spectrum is the most crucial for identification purposes. Many functional groups have specific Raman shifts within the fingerprint region. For example, carbonyl (C=O) stretches often appear around 1600-1800 cm^{-1}, while C–C and C–N stretches frequently occur in the range of 1000-1500 cm^{-1}. Double bonds between carbon atoms (C=C stretching vibrations), such as those found in alkenes and aromatic rings, usually exhibit Raman shifts around 1500-1650 cm^{-1}. These specific vibrations help with identifying the functional groups present in the organic molecule (Schrader, 2008).

The silent region in Raman spectroscopy typically refers to the range from 1800 to 2800 cm^{-1}. This area is called "silent" because it usually lacks significant Raman-active vibrational modes for most organic

molecules. As a result, it appears relatively featureless in Raman spectra, making it less useful for identifying specific compounds or functional groups.

And the last region is the C-H stretching region, which spans from approximately 2800 to 3100 cm^{-1}. This part of spectrum is also quite significant because it contains vibrational modes associated with the stretching of carbon-hydrogen (C-H) bonds. These vibrations are present in almost all organic compounds, making this region highly informative for the analysis of hydrocarbons and other organic substances. There are different types of C-H bonds: aliphatic C-H and aromatic C-H stretches. These two types exhibit distinct spectral features that allow for their differentiation. Aliphatic C-H stretching vibrations typically appeared in the range of 2800-3000 cm^{-1}, for example, methylene ($–CH_2–$) stretching was observed around 2840-2935 cm^{-1} or methyl ($–CH_3$) appeared near 2860-2960 cm^{-1} (Zhang et. al., 1996). These stretches usually looks like sharp and well-defined peaks. Multiple peaks may also appear in this region, corresponding to the different types of aliphatic C-H bonds. Aromatic C-H stretching vibrations are typically found slightly higher in the range of 3000-3100 cm^{-1} (Šebek et. al., 2013).

4.3. Advantages and limitations

Raman spectroscopy is a powerful widely used analytical technique. However, despite its versatility and utility, it also faces several limitations and challenges that can affect its performance and application. The text below will give specific examples and detail some of the challenges.

Significant challenge arises from fluorescence. It can overwhelm the weaker Raman signals, reducing the SNR (signal-to-noise ratio) and complicating the detection and analysis of Raman peaks. The intense fluorescence background can obscure critical spectral features of the target compounds, leading to difficulties in characterizing and quantifying these components.

Fluorescence is a process that begins with the absorption of high-energy photons by a molecule, which excites its electrons to a higher electronic state. This absorption typically requires photons in the UV or visible spectrum. When a molecule absorbs a photon, it transitions from its ground electronic state S_0 to a higher state S_1. Subsequently, the molecule relaxes from this higher vibrational state $n_1 > 0$ to the zero vibrational level $n_1 = 0$ within the excited state S_1. After reaching a zero vibrational level of the excited state, the molecule emits photon and returns to its ground electronic state $n_0 = 0$ on S_0 state (Harvey, 2011).

Emitted photon is observed as fluorescence. The wavelength of the emitted fluorescence is typically longer (lower energy) than the absorbed photon due to the loss of energy during the non-radiative relaxations. The fluorescence emission occurs at a specific frequency characteristic of the molecule and is highly dependent on the excitation wavelength. Unlike Raman scattering, where the shift in

wavelength is independent of the laser's wavelength, fluorescence emission is fixed in frequency relative to the excitation wavelength. Fluorescence occurs simultaneously with Stokes Raman scattering upon laser excitation because red-shifted Stokes Raman scattering overlaps with fluorescence emission. However, this problem does not affect anti-Stokes Raman scattering, as it is blue-shifted relative to the excitation wavelength, thus avoiding spectral overlap with fluorescence. The issue is more pronounced when visible light is used for excitation. The intense fluorescence signal in Raman spectroscopy significantly impacts the accuracy and sensitivity of Raman measurements (Wei et. al., 2015).

Numerous factors influence the fluorescence intensity and spectral characteristics of clay minerals. Transition metal ions, such as iron (Fe) and manganese (Mn), impurities or structural constituents, can enhance fluorescence emission. Structural defects within the clay structure also contribute to fluorescence properties. The presence of organic matter, such as humic substances or organic inclusion, associated with clay minerals can further affect fluorescence. Organic molecules interact with clay surfaces, altering the mineral's electronic structure and influencing fluorescence emission. Additionally, environmental factors such as pH, temperature, and humidity can affect fluorescence properties by modulating surface interactions (Gates et. al., 2017).

Similar fluorescence behavior can indeed be observed in the Raman spectra of certain organic compounds, particularly those featuring aromatic or conjugated π-electron systems (Cloutis et. al., 2016). These compounds possess the ability to emit fluorescence when excited by the Raman laser, leading to background fluorescence that may interfere with Raman signals. Polycyclic aromatic hydrocarbons (PAHs), composed of multiple aromatic rings, aromatic amino acids like tryptophan, tyrosine and phenylalanine are known to fluoresce under specific conditions.

Another challenge in Raman spectroscopy is presence of water in samples that can significantly impact the accuracy and clarity of spectral analysis. This issue is particularly pronounced in hygroscopic materials, which readily absorb moisture. Raman bands of water, notably the O-H stretching vibrations around 3200-3600 cm^{-1}, can alter the intensity of the Raman peaks of the studying material. Moisture can quench fluorescence effect of certain materials leading to baseline variation and spectral changes, this problem was studied by Hossain et. al., 2019 for quantitative pharmaceutical analytical applications.

Analyzing organic compounds using Raman spectroscopy can pose other unique challenges. In general, organics tend to be more sensitive to temperature and environmental changes. These compounds often contain reactive functional groups, which are more susceptible to environmental factors such as moisture, oxidation, and exposure to light. These can lead to changes in molecular structure or molecular degradation.

The detailed experimental data provided by Raman spectra are specific to individual molecules and, in many cases, to their geometries. Raman spectroscopy has been utilized to differentiate between

crystalline polymorphs and the orientation of polymers, though the variations between these spectra are typically minor. Malenfant et al., 2024 describe problem of structural ambiguities. Different structural isomers or conformers of the same molecule can produce different Raman spectra. Without reference data, distinguishing between these structural variations becomes difficult. Another problem can occur with larger or more complex organic molecules exhibiting numerous vibrational modes. These modes can interact and produce overlapping peaks, complicating the assignment of specific vibrations to distinct peaks. Fortunately, the problem is partially solved with theoretical calculations and computational chemical methods.

One of the parameters for measuring quality of the spectral data is SNR or signal-to-noise ratio. It represents the ratio of intensity of the Raman signal to intensity of the background noise. A high SNR value indicates that the Raman signal is much stronger than the noise, and conversely, a low SNR means that the noise is relatively high compared to the signal, which can obscure the Raman peaks and make interpretation difficult (Mccreery, 2005). Not only background fluorescence can affect SNR value, but also laser power, detector sensitivity or sample concentration. Signal-to-noise ratio can be calculated in different ways, there are two common metrics: SNR (RMS or Root Mean Square) and SNR (PP or Peak-to-Peak)

SNR (RMS) is a measure of the signal strength relative to the average level of noise, calculated using the root mean square method, where $I\ signal$ is the intensity of Raman signal and $\sigma\ noise$ is the standart deviation of the noise (RMS noise level).

$$\text{SNR (RMS)} = \frac{I\ signal}{\sigma\ noise}$$

SNR (PP) is calculated comparing the peak signal to the peak noise level, where $I\ signal$ is the intensity of Raman signal and $N\ peak - to - peak$ is the difference between maximum and minimum noise levels.

$$\text{SNR (PP)} = \frac{I\ signal}{N\ peak - to - peak}$$

SNR PP method normally gives lower values, considering the spectrum as worse than SNR RMS method does. In addition to SNR other parameters are also used to evaluate the quality of Raman spectrum including baseline stability, wavenumber accuracy, FWHM (full width at half maximum) etc.

4.4. Raman spectroscopy in the field of exobiology

Before the deployment of the Perseverance rover with its SHERLOC instrument (Scanning Habitable Environments with Raman and Luminescence for Organics and Chemicals), there were significant

efforts and developments in using Raman spectroscopy for Mars exploration through laboratory simulations and testing in Mars analog environments on Earth.

First of all, contributions from previous missions should be mentioned. Curiosity rover with instruments like the ChemCam (Chemistry and Camera Complex) demonstrated the effectiveness of laser-based techniques in planetary exploration, this success later influenced the development and integration of Raman spectrometers in subsequent missions. Although Curiosity isn't equipped with Raman spectrometer it uses laser-induced breakdown spectroscopy. Laser-Induced Breakdown Spectroscopy and Raman Spectroscopy are both laser-based analytical techniques used to determine the composition of materials, but they operate on different principles and have distinct applications. While Raman is used for molecular and chemical analysis (for identification of specific compounds, including minerals, organic molecules, and complex biochemical substances), LIBS is primarily used for elemental analysis (for detection a wide range of elements, including trace ones). Principles are also different: LIBS spectroscopy uses a high-powered laser pulse to ablate an amount of material from the sample, creating a plasma. As the plasma cools, the excited atoms and ions emit light at characteristic wavelengths, which is detected and analyzed to determine the elemental composition of the sample. So, its a slightly destructive technique in comparison to Raman spectroscopy. Both techniques face their own challenges: LIBS can be affected by matrix effects and requires calibration, while Raman can be affected by fluorescence. These techniques are complementary and, when used together, can provide a comprehensive analysis of a sample's composition. This is why, for example, the Perseverance rover uses both LIBS and two Raman spectrometers to maximize its scientific capabilities (532 nm excitation for SuperCam and 248.6 nm for SHERLOC). By utilizing these two complementary Raman spectrometers, the Perseverance can conduct a comprehensive analysis of the Martian surface, combining remote sensing capabilities with detailed close-up investigations.

SuperCam is mounted on the rover's mast and combines multiple analytical techniques, including LIBS, Raman spectroscopy, visible and infrared (VISIR) reflectance spectroscopy, and remote micro-imaging. SuperCam uses a 532 nm laser, which allows it to excite Raman signals from the surface of rocks and soil on a distance. The laser fires pulses at the target, and the backscattered light is collected and analysed, generating Raman spectra. This remote sensing capability enables SuperCam to analyze the composition of distant targets without the need to physically approach them.

SHERLOC (Scanning Habitable Environments for Raman and Luminescence for Organics and Chemicals) is a robotic instrument onboard the Perseverance rover that operate in Jezero crater site on Mars. Its equipped with 248.6 nm pulsed laser for surface scanning and collecting photons emitted from Raman scattering and fluorescence of near-surface materials. SHERLOC's main purpose is to identify organic materials but is designed for the analysis of inorganic phases as well by examining the Raman peaks 800 and 4000 cm^{-1}. By employing a deep ultraviolet (DUV) laser, SHERLOC captures inherent

fluorescence emissions from aromatic organic compounds, along with Raman scattered photons from molecules that facilitate the identification of functional groups within organics, minerals and chemicals. SHERLOC captures high-resolution color and grayscale images of both natural and abraded samples on the surface (Bhartia et. al., 2021). Additionally, recently was reported by Phua, et al., 2024 that the 248.6 excitation allows to acquire Raman spectra of sulphate minerals without significant fluorescence.

Hollis et. al., 2021 obtained spectra with SHERLOC Brassboard instrument at the NASA Jet Propulsion Laboratory, which is custom deep ultraviolet spectrometer, designed to be optically similar to the flight SHERLOC instrument. The Brassboard device serves as a terrestrial analogue to the SHERLOC flight instrument aboard Perseverance, employing comparable optical pathways and components to guarantee that its results are close to those obtained by SHERLOC during the mission. Brassboard's spectral library contains more than 90 spectra of different materials geologically relevant to the ones expected to be present at the Perseverance landing site. It contains spectra of evaporites, silicates and diagenetic minerals (Fig. 9).

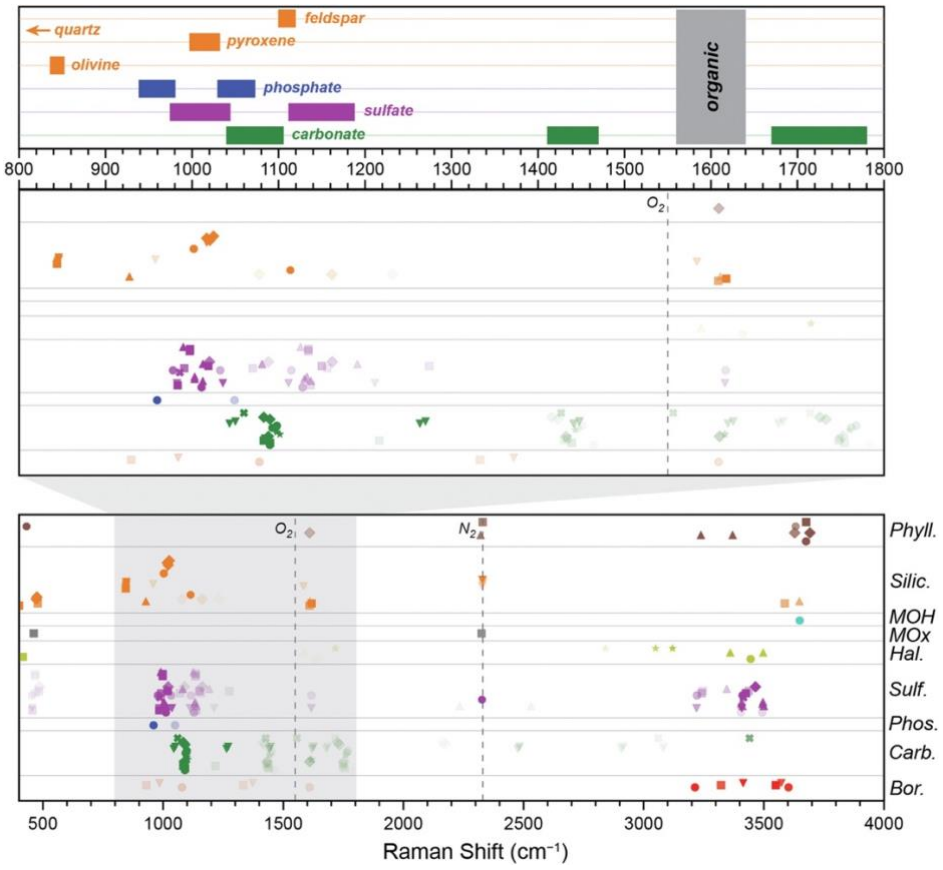

Fig. 9. Spectral library obtained using SHERLOC Brassboard (Hollis et. al., 2021)

4.5. Previous research

A notable study in this field was made by Vítek et. al., 2009a. Authors explored the use of Raman micro-spectroscopy for detection β-carotene in experimentally prepared evaporitic matrices. This study

involved mixing β-carotene with powdered gypsum ($CaSO_4 \cdot 2H_2O$), halite (NaCl), and epsomite ($MgSO_4 \cdot 7H_2O$). Analysis was performed on a Renishaw InVia Reflex Raman micro-spectrometer with 785 nm excitation, a standard 50x lens objective that provides a spot size of ≈ 2 μm was used. For samples with 100, 10, 1 and 0.1 mg/kg β-carotene concentration the laser power was set to 15 mW. Samples were homogenized in an agate mortat. According to authors, clear β-carotene C=C band (1515 cm^{-1}) was detected in gypsum matrix at concentration level of 10 mg/kg. Spectral signatures were observed even at concentrations as low as 1 mg/kg.

Subsequent research by Vítek et. al., 2009b was designed to compare detection limits of β-carotene using 785 and 514.5 nm excitation. Analysis was performed on a same micro-spectrometer as it was in previous study. Laser power was set to 2 mW for 514.5 nm excitation and 15mW for 785 nm. In this study characteristic Raman bands of β-carotene were detected at concentration under 1 mg/kg using 514.5 nm excitation and at interval 1–10 mg/kg using 785 nm laser excitation (Fig. 10).

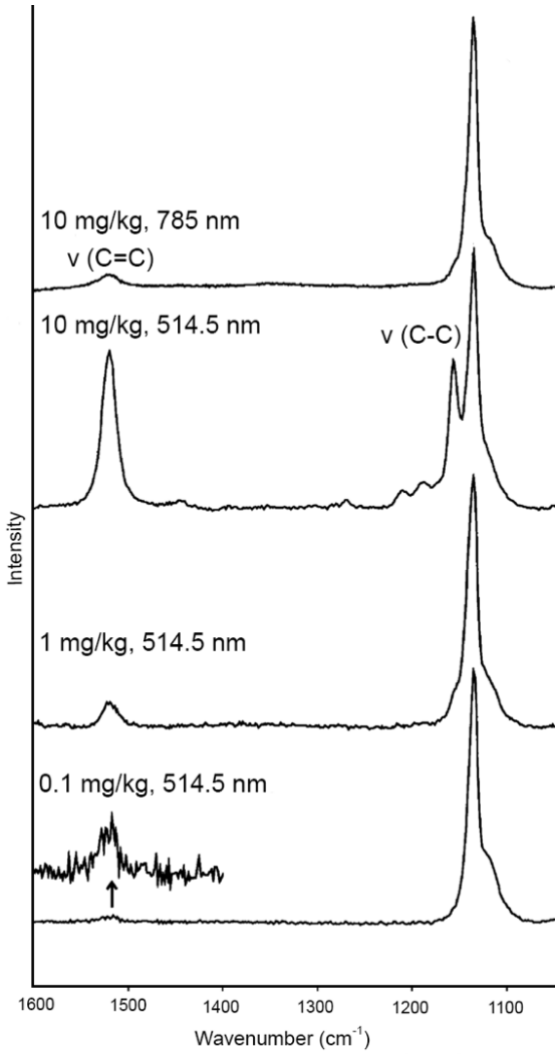

Fig. 10. Comparison of 785 and 514.5 nm excitation for detection different β-carotene concentrations (modified from Vítek et. al., 2009b)

5. Materials and methods

5.1. Materials

Pure laboratory standards of β-carotene (Sigma-Aldrich) and $CaSO_4 \cdot 2H_2O$ (Penta chemicals) were used for the experiment.

Selection of appropriate clays was more difficult and important. We had chosen 2 distinct geological samples: Sedlec Ia kaolin from deposits of the Karlovy Vary region in Czech Republic and GMZ bentonite from Gaomiaozi deposit in Inner Mongolia, China.

From the theoretical framework described earlier, it can be concluded that kaolinite, as a representative of the kaolin group, may be quite relevant to our experiment. According to Sedláčková, 2019 analysis of standardized composition of Sedlec Ia kaolin, main compounds in weight percentage are: SiO_2 - 47.4%, Al_2O_3 - 37%, K_2O - 0.97% and Fe_2O_3 - 0.89%. Author also describes mineralogical composition of Sedlec Ia kaolin: kaolinite - 91%, quartz - 2%, and micas - 7%.

GMZ bentonite was selected to provide a contrasting spectral output to kaolin and is known for its different chemical and physical properties, higher CEC.

According to Zhang et al., 2021 XRD analysis of GMZ bentonite, it is predominantly composed of montmorillonite. 2θ values of diffraction peaks are at 6.03°, 20.0°, 35.0° (d-spacing 14.7, 4.44 and 2.5 Å). The ones indicating quartz, cristobalite and albite are at 26.8°, 22.2°, 28.1°.

5.2. Methods

Before starting the main experiment, we made X-ray diffraction analysis, pXRF and Raman measurement of selected clay minerals to evaluate the expected level of fluorescence.

X-ray diffraction analysis was performed using a PANalytical X'Pert Pro diffractometer with a Cu anode, operating at a tube voltage of 40 kV and a tube current of 30 mA.

XRD analysis of Sedlec Ia kaolin and bentonite GMZ is consistent with earlier reported data. In kaolin sample kaolinite and muscovite were detected as the primary components (Fig. 11). The high percentage of kaolinite confirms its dominance in the sample, while the presence of micas aligns with the identification of muscovite.

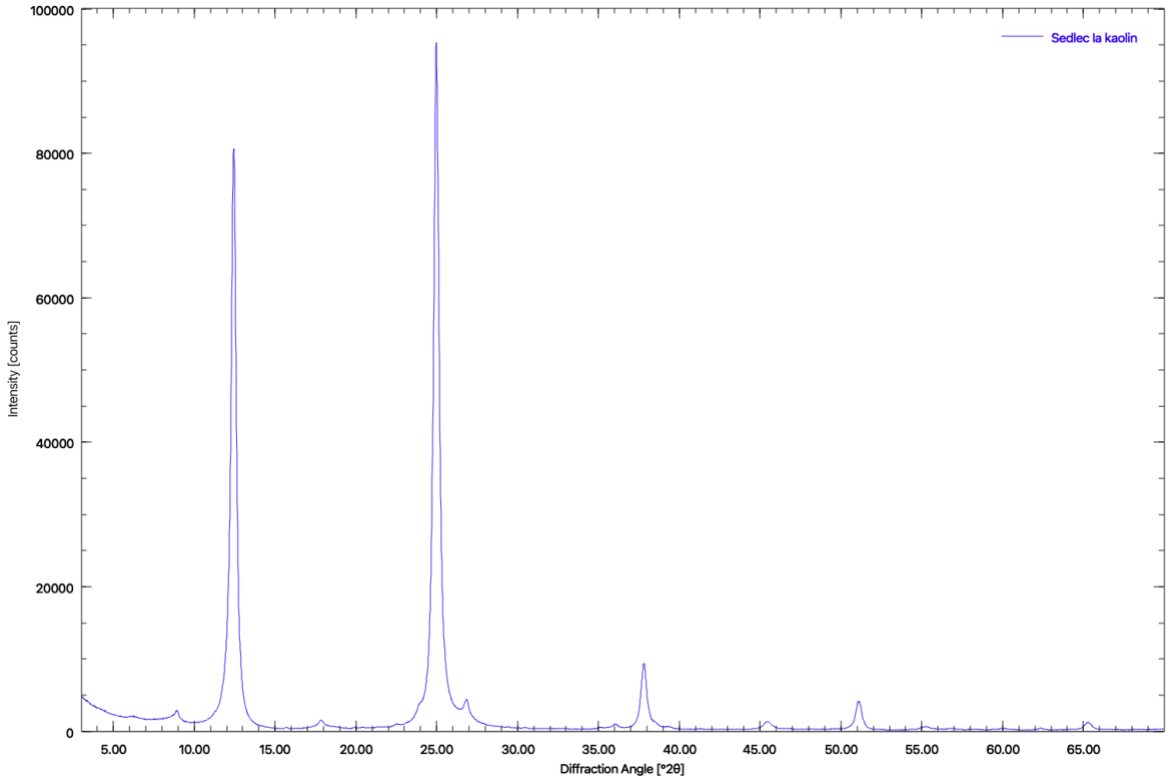

Fig. 11. XRD analysis of Sedlec Ia kaolin

In bentonite GMZ sample quartz with diffraction peak at 26.6°, cristobalite at 22° (with the corresponding d-spacings of 3.35 and 4.04 Å respectively) were detected (Fig. 12). Diffraction peaks of montmorillonite were slightly shifted with main peaks at 5.9° and 34.9° (d-spacing of 15.02 and 2.57 Å).

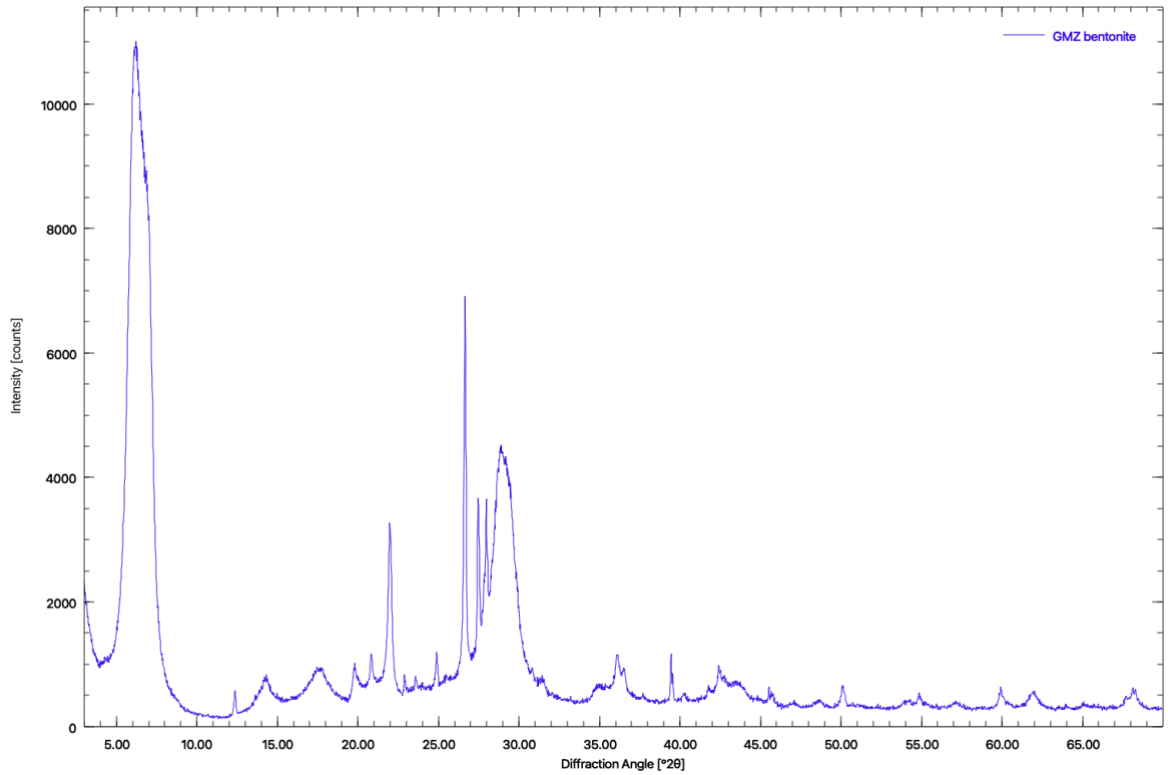

Fig. 12. XRD analysis of GMZ bentonite

Raman spectra were acquired by handheld Raman spectrometer EnSpectr RaPort (Enhanced Spectrometry, Inc., San Jose, CA, USA). It is designed as a "pistol-like" instrument that weighs ca. 2 kg, and is equipped with a Nd:YAG frequency-doubled 532 nm wavelength laser. The system was operated on batteries and controlled via a USB 2.0 port connection with a laptop running software allowing a wide range of experimental settings. Spectra were recorded in the range of 190 – 3375 cm^{-1} with the same measurement parameters that will be used in the main experiment (100 ms x 100 accumulation, laser attenuation 40). The laser power setting (attenuation parameter of 40) corresponds to 25mW at the sample as confirmed by the LaserCheck power meter (Coherent, Santa Clara, CA). Data was processed in OPUS spectroscopy software created by Bruker.

Fluorescence intensity (similarly to the intensity of Raman bands) is dependent not only on the sample studied, but also on the type of spectrometer and chosen experimental settings, nevertheless we compared the fluorescence intensity of different clay minerals while all other significant parameters were similar.

From data illustrated on Fig. 13, it is evident that the background fluorescence of kaolin exceeds that of bentonite by approximately 6x. The maximum intensity was determined to be 39,500 a.u. for kaolin and 6,600 a.u. for bentonite. This indicates that we have chosen 2 significantly different samples of clays, representing vastly different levels of fluorescence. This, in turn, will allow us to test detectability of the pigment across a wider range of fluorescence levels. For greater clarity and understanding of the scales

we will be working with, we additionally measured several standards of clay minerals: Ca-montmorillonite, Na-montmorillonite, and illite. The absolute highest fluorescence was observed in Ca-montmorillonite, with an 50,200 a.u. intensity. The selected GMZ bentonite exhibits the lowest intensity values from all tested clay minerals. The actual Raman bands of clay minerals were not detected in this study using the 532 nm excitation, further documenting the fluorescence issue linked to clay minerals using Raman spectroscopy with excitation in the visible range.

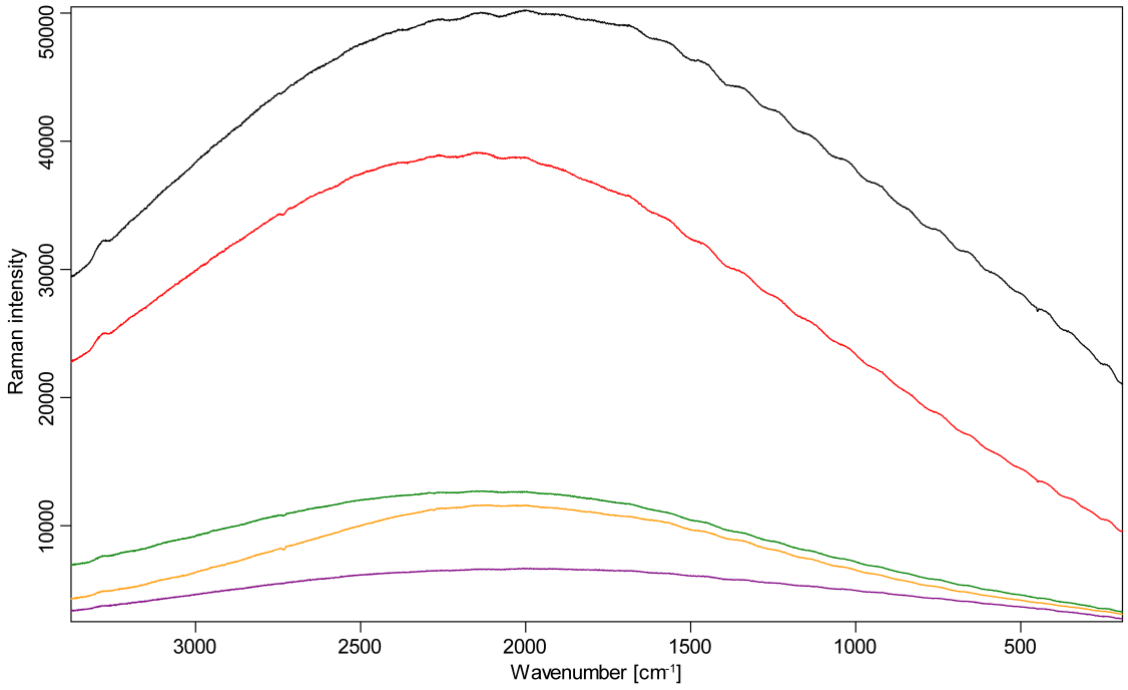

Fig. 13. Raman spectra of selected clays (black: Ca-montmorillonite, red: Sedlec Ia kaolin, green: Na-montmorillonite, orange: illite, purple: GMZ bentonite)

As an additional analytical method, which we utilized trying to explain fluorescence variation, was pXRF of clays measured by Niton™ XL3t GOLDD+ XRF Analyzer (Fig. 14). From the measurements, it was noted that the Sedlec Ia kaolin sample had higher concentration of arsenic and lead compared to the GMZ bentonite sample. For Pb the value was more than 10x higher: 350.1 versus 31 ppm. For As almost 4x: 23.7 versus 6.2 ppm. Higher phosphorus concentration also was detected.

In contrast, analysis showed a significantly higher strontium content in the bentonite, approximately 5x higher Sr: 479.8 versus 114.7 ppm in kaolin sample. A more sensitive analysis for the presence of lanthanides, which could increase the overall fluorescence background, was not conducted. Possibly, increased concentration of REEs could explain higher spectral background.

	concentration in kaolin (ppm)				concentration in bentonite (ppm)		
	x	**min.**	**max.**		**x**	**min.**	**max.**
As	23.7	20.4	26.9	**As**	6.2	4.9	7.4
Pb	350.1	345.6	354.6	**Pb**	31.0	29.5	32.6
Cu	11.7	8.2	15.2	**Cu**	69.2	65.2	73.3
Bi	47.3	45.2	49.3	**Bi**	< LOD		
Cd	14.1	12.5	15.7	**Cd**	17.0	15.3	18.8
Mg	< LOD			**Mg**	16235.4	14974.8	17496.0
Al	204604.3	203539.7	205668.8	**Al**	77547.1	76368.4	78725.8
Si	316777.1	316141.5	317412.7	**Si**	437119.2	433957.3	440281.2
P	484.3	390.7	579.0	**P**	< LOD		
S	1159.2	1126.5	1191.9	**S**	749.4	716.1	782.7
Cl	< LOD			**Cl**	501.9	484.8	519.0
K	13040.0	12942.9	13137.0	**K**	6007.6	5901.9	6113.3
Ca	5664.1	5567.2	5761.0	**Ca**	10735.6	10545.3	10925.9
Ti	1476.8	1453.0	1500.7	**Ti**	1017.7	994.2	1041.2
V	68.1	56.2	80.0	**V**	40.7	30.5	50.8
Cr	187.6	180.8	194.4	**Cr**	144.9	137.4	152.4
Mn	125.2	112.8	137.5	**Mn**	297.5	283.2	311.8
Fe	10362.6	10304.1	10421.1	**Fe**	29701.0	29126.7	30275.2
Co	70.6	55.0	86.2	**Co**	173,12	147.7	198.5
Zn	43.0	40.6	45.4	**Zn**	70.3	67.7	73.0
Rb	86.6	85.9	87.3	**Rb**	51.9	51.0	52.9
Sr	114.7	113.6	115.9	**Sr**	479.8	477.6	482.0
Zr	87.3	86.4	88.2	**Zr**	173.2	171.1	174.8
Nb	27.1	26.5	27.7	**Nb**	66.4	61.7	71.1
Mo	12.7	12.1	13.3	**Mo**	16.0	15.1	16.9
Pd	8.2	7.3	9.2	**Pd**	8.2	7.2	9.2
Ag	5.5	4.6	6.4	**Ag**	6.6	5.6	7.6
Sn	27.3	24.4	30.1	**Sn**	18.0	15.0	21.0
W	55.2	41.6	68.8	**W**	39.6	32.2	46.9
Hg	6.5	4.6	8.5	**Hg**	< LOD		
Th	39.4	37.7	41.0	**Th**	22,16	21,015	23,305
U	< LOD			**U**	15,37	13,765	16,975

Fig. 14. pXRF data on Sedlec Ia kaolin and bentonite GMZ in ppm (x: measured value, max.-min.: measurement error)

5.3. Sample preparation and measurement

We started preparation of samples by creating 5 primary powdered mixtures of selected clay and gypsum in varying ratios. The specific ratios used were 10 wt%, 30 wt%, 50 wt%, 70 wt% and 90 wt% of clay respectively. The raw materials were carefully weighed, and mixed to achieve uniform distribution of clay and gypsum particles. This initial step was crucial as it established the primary mixtures that would be used for subsequent experimental procedures.

One of the critical challenges we faced during the sample preparation process was achieving sufficient homogenization. Homogenization is essential to ensure that each sample is uniformly mixed, which directly affects the accuracy and reliability of the subsequent analytical results. Initially, we experimented with several different techniques and later tried an electric grinder BOSCH TSM6A013B,

equipped with blade knives (wattage is 180 W). The high-speed grinder's blades significantly improved the uniformity of the mixtures. By homogenizing the samples in short bursts with average grinding time 90 sec per sample, we were able to achieve a fine, consistent powder where components were relatively evenly distributed. The spectral data from the samples mixed with the grinder were markedly more consistent compared to those mixed using other methods. We continued by preparing the highest concentration from which subsequent dilutions to lower concentrations would be made. The upper chosen concentration was 50 ppm of pigment. Accordingly, we created 5 'donor' mixtures with different wt% of clay: 10, 30, 50, 70, and 90. The 50 ppm β-carotene mixtures were served as the base, diluted samples were created by mixing them with the primary clay-gypsum mixtures. Afterwards, another round of mixing was conducted in the grinder. This method allowed us to produce a series of samples with progressively decreasing pigment concentration while maintaining the initial clay wt%. Each dilution step was carried out meticulously to ensure accurate concentration levels. Fully understanding a risk of certain loss in accuracy during dilution, these losses were nevertheless assessed as minor compared to inaccuracies in manually weighing pigment at lower concentrations.

After achieving sufficient homogenization, the next step involved converting the powdered samples into solid forms. We processed the powdered mixtures using a hydraulic press Trystom H-62 to make round pellets 13 mm in diameter and 1 mm in thickness (Fig. 15). For each pellet were used ~ 250 mg of powder and 2 pellets (duplicates) per sample were made in order to control homogeneity. The hydraulic press allowed us to compact the powder into dense, round pellets with consistent size and shape. Powdered samples were subjected to ~ 55kN pressure.

Fig. 15. Step-by-step preparation of pellets using hydraulic press

The idea to prepare samples in the form of pellets in our research didn't come without conscious choice. It was specifically inspired by the methods that will be employed by the Rosalind Franklin Rover as part of the ExoMars mission. This rover will collect Martian soil and rock samples, process them into fine powders, and form them into pellets for precise and comprehensive analysis.

Pressures too low resulted in pellets that were fragile and prone to breaking, while excessively high pressures could cause the pellets to crack. Interestingly, that pellets containing kaolinite made under identical parameters as ones with bentonite were significantly more fragile and mechanically unstable. Nevertheless, pellets were smooth and uniform, providing a reliable surface for subsequent spectroscopic measurements.

Process of pelletizing the powder also improved the reproducibility of results. By ensuring that each pellet had a consistent density and surface texture, we minimized potential variations in spectral data that could arise from irregularities in the sample surface. The created pellets were stored in the freezer to prevent potential pigment degradation.

Prepared pellets were analyzed using EnSpectr RaPort – handheld Raman spectrometer using 532 nm laser for excitation (Fig. 16).

Fig. 16. EnSpectr RaPort handheld Raman spectrometer and process of measuring pellets

The instrument was operated via cable connection by laptop computer. The measurement range was 190–3375 cm^{-1}. Each spectrum was recorded using the following parameters: an integration time of 100 ms with 100 accumulations. The laser had an experimentally verified spot size of ≈ 50 µm (Fig. 17). The laser attenuation was set to 40, corresponding to an estimated power of 25 mW at the sample.

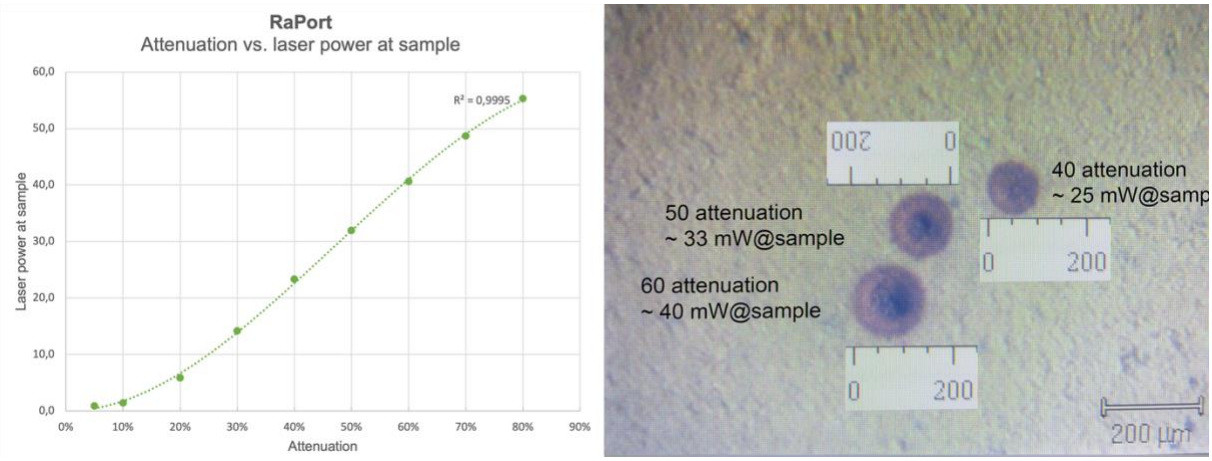

Fig. 17. Left: graphical demonstration of attenuation vs. laser power at sample (in mW) for EnSpectr RaPort spectrometer. Right: Spot size of RaPort 532 nm laser experimental check

Each pellet was measured at 10 different points evenly distributed across its surface. In result, we got 20 measurements per sample (considering 2 pellets were prepared for each mixture).

Then, 20 spectral measurements were processed using the already mentioned OPUS software by Bruker. For standardization and uniformity of processing, baseline correction was always performed via interactive mode using straight lines method and the maximum number of attenuations. The intensity of the β-carotene peak (1512 cm^{-1}) and the peak of gypsum (1008 cm^{-1}) were measured.

Obtained numerical data later was statistically processed in Excel and R Program software. Graphical outputs for Results chapter were prepared using R Program and PyCharm.

6. Results

As references for subsequent analyses pure spectra of gypsum and β-carotene are shown on Fig. 18. β-carotene exhibits two strong Raman bands around 1512 and 1157 cm^{-1}, which are attributed to the stretching vibrations of the polyene chain's C=C and C–C bonds, respectively. Raman spectrum of gypsum is characterized by several distinct peaks, the strongest is around 1008 cm^{-1}, corresponding to the symmetric stretching of sulfate (SO_4^{2-}) group. In the folowing text we will demonstrate the results of our main experiment, where intensity of pigment and gypsum peaks will be suppressed by the fluorescence of the clay minerals.

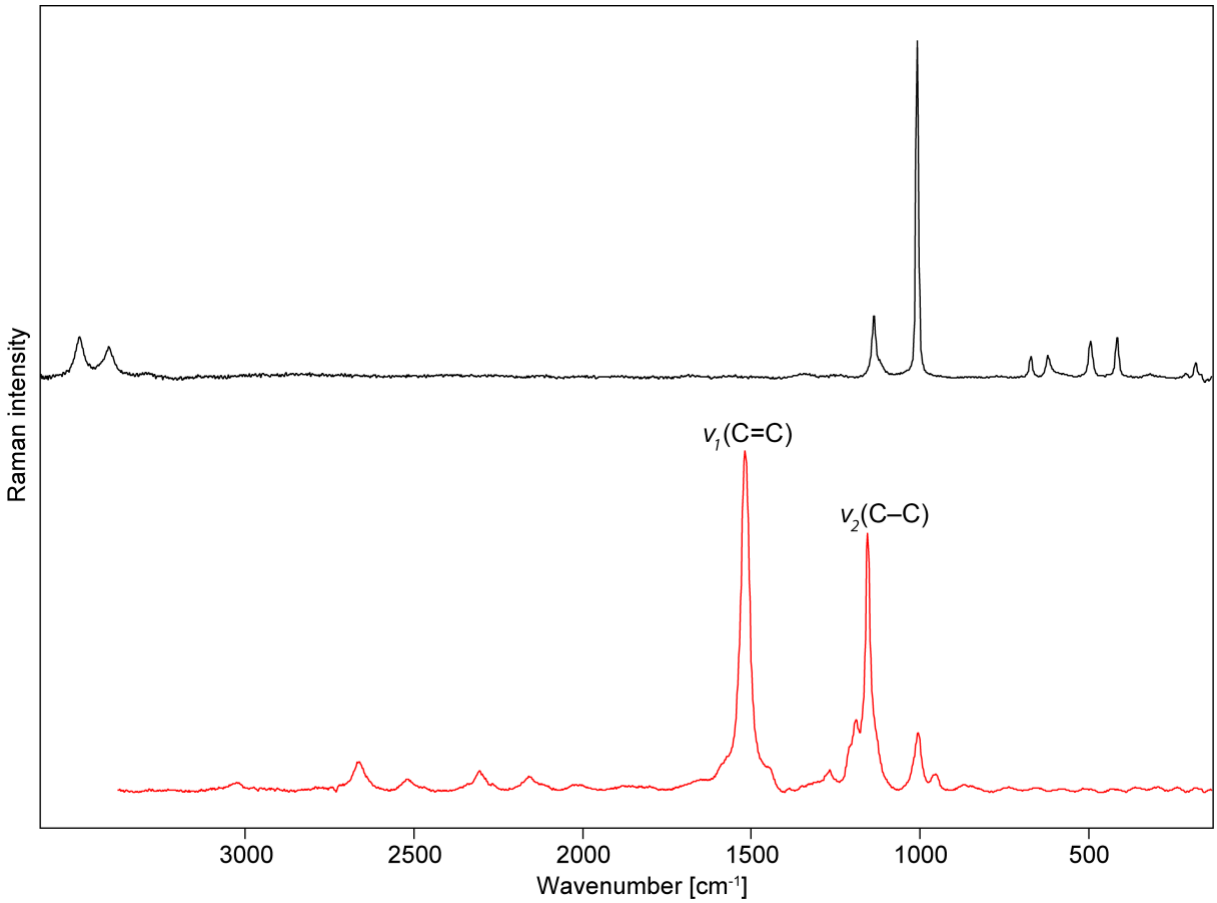

Fig. 18. Raman spectra of pure gypsum ($CaSO_4 \cdot 2H_2O$, top) and pure β-carotene (bottom). Both spectra were acquired with RaPort handheld spectrometer and baseline corrected

The analysis of different β-carotene concentration levels reveals some trends in how the Raman signal of pigment deteriorates with increasing kaolin wt% in the mixture. Across all concentrations, there is a consistent decrease in β-carotene signal intensity as the proportion of kaolin in mixture rises. This trend underscores the significant impact of kaolinite's fluorescence, the primary component of kaolin, which increasingly masks weaker Raman signal.

Mean values tend to be higher because they are influenced by extreme values. They provide an indication of the overall signal intensity and show a smoother and more gradual decline in detectability. The presence of higher values can mask the impact of fluorescence, potentially giving an overestimated perception of pigment detectability. At 50 ppm of β-carotene, the mean signal of pigment remains detectable even at 90 wt% of kaolin, though it is significantly reduced (Tab. 1). Then, at lower concentrations as 35 ppm and 20 ppm are, it disappears at 90 wt% and 70 wt% of kaolin, respectively. For lowest β-carotene concentrations as 10 ppm and 5 ppm are, there is no signal for mixtures with 70 wt% and 30 wt% of kaolin, respectively (Fig. 19).

	50 ppm	35 ppm	20 ppm	10 ppm	5 ppm
10 wt% of K	1408.9	783.2	468.0	174.5	35.1
30 wt% of K	819.7	404.4	237.0	62.3	0
50 wt% of K	502.1	321.7	99.7	30.3	0
70 wt% of K	294.6	211.4	10.0	5.9	0
90 wt% of K	43	0	0	0	0

Tab. 1. Mean Raman intensity of β-carotene peak at 1512 cm^{-1} in the kaolin-gypsum mixture

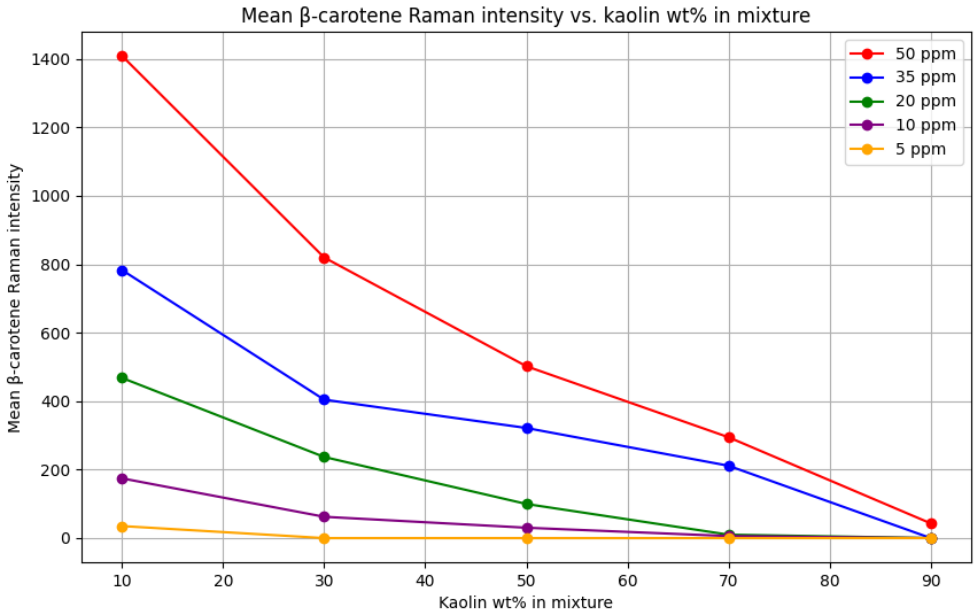

Fig. 19. Mean Raman intensity of β-carotene peak at 1512 cm^{-1} in the kaolin-gypsum mixture

Median values represent the central tendency of the data without being influenced by outliers. They offer a more robust measure of typical signal intensity, reflecting detectability more accurately under normal conditions. According to median values, at 50 and 35 ppm of β-carotene, pigment is already not detectable in the mixture with 90 wt% of kaolin (Tab. 2). For 20 ppm it is limited by 70 wt% of kaolin.

At 10 ppm of pigment it was detectable only at 10 wt% of clay in mixture (Fig. 20). Median values are zero for all clay ratios at 5 ppm concentration level. Median values illustrate more abrupt decrease in detectability. They accurately show when β-carotene becomes undetectable, reflecting the more typical scenario of the signal being obscured by fluorescence. Summarizing, medians can give us a clearer view of when pigment becomes truly undetectable.

	50 ppm	35 ppm	20 ppm	10 ppm	5 ppm
10 wt% of K	1255.5	753.4	404.5	189.3	0
30 wt% of K	718.5	395.0	205.0	0	0
50 wt% of K	448.2	311.0	69.2	0	0
70 wt% of K	267.4	206.5	0	0	0
90 wt% of K	0	0	0	0	0

Tab. 2. Median Raman intensity of β-carotene peak at 1512 cm^{-1} in the kaolin-gypsum mixture

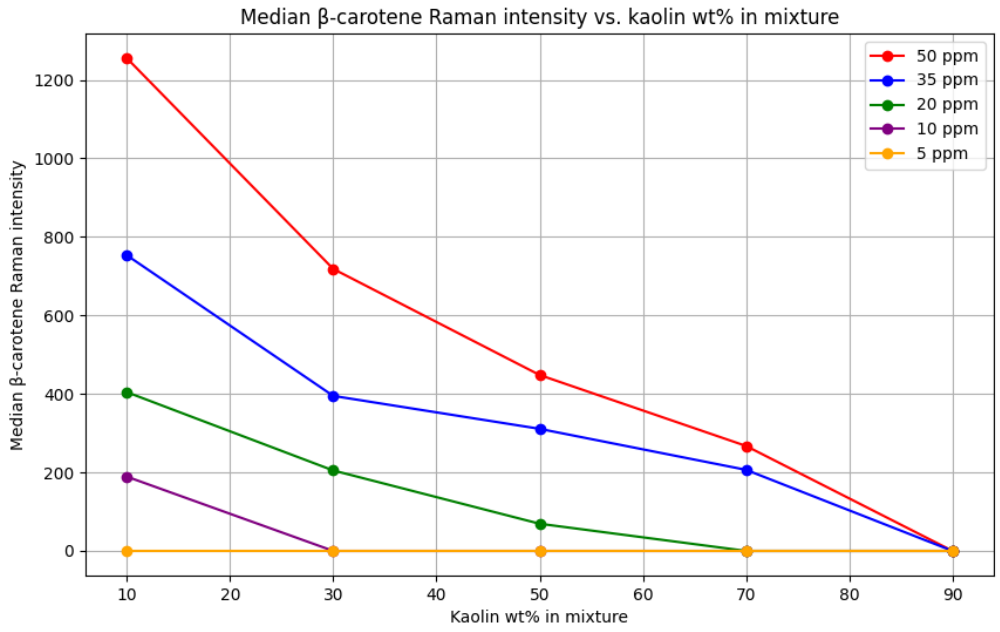

Fig. 20. Median Raman intensity of β-carotene peak at 1512 cm^{-1} in the kaolin-gypsum mixture

Furthermore, the rate of decrease in Raman signal intensity appears to be faster than linear, suggesting nonlinear trend. Especially, in the measured data, we observe a significant drop in signal intensity in the initial (e.g., from 10 to 30 wt% of clay) and last interval (from 70 to 90 wt% of clay). Even though some values are zero, in a theoretical experiment with more data, these zeros could represent very small values close to zero.

Nevertheless, the most suitable function to approximate the data might be the exponential decay function. Here are a few reasons why: exponential decay provides a smooth and continuous curve, which

fits well with the gradual decline observed both in the mean and median values. While the hyperbolic decay function can also describe rapid decreases, it might not level off as appropriately to zero as an exponential function does. Power-law and logarithmic functions typically describe different types of decay and might not fit the data, given the rapid initial decrease and data leveling off later. For demonstration, there is a comparison of hyperbolic and exponential decay approximation for mean 50, 35, 20 and 10 ppm data shown on Fig. 21.

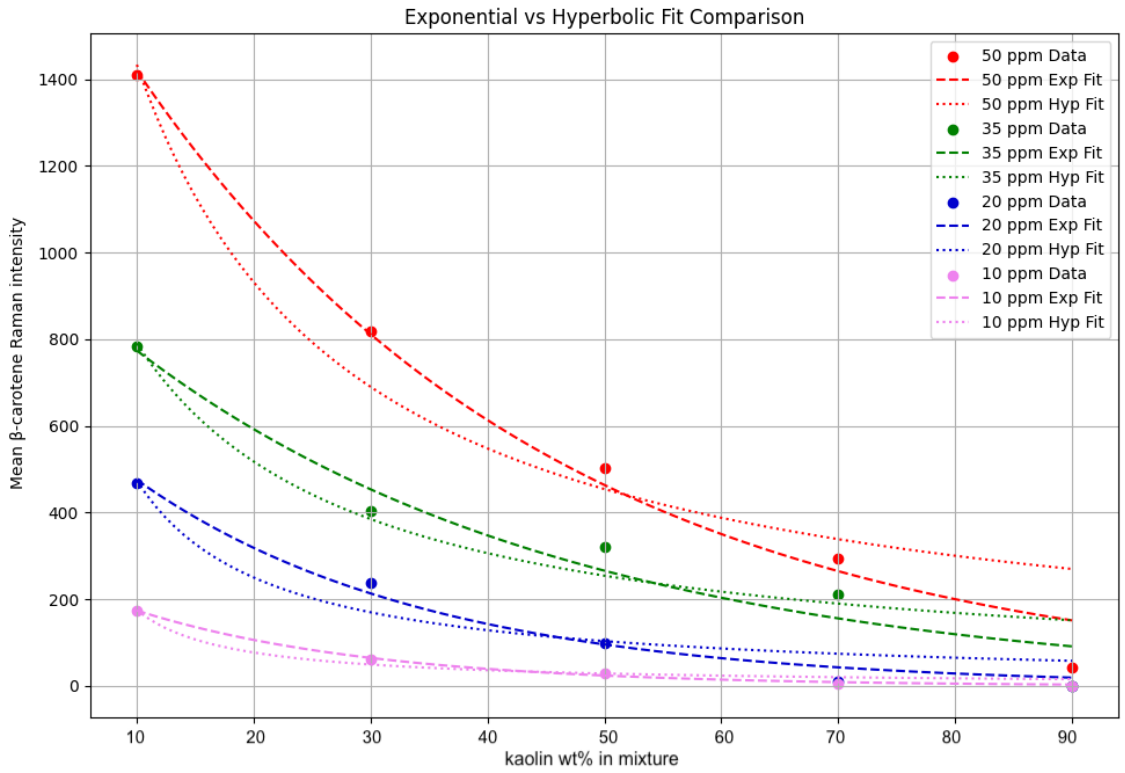

Fig. 21. Comparison of exponential and hyperbolic model for mean data approximation (zero values were replaced with values extremely close to zero)

We conducted a similar experiment using bentonite GMZ. Preliminary analysis revealed that this bentonite fluoresces less than kaolin. In comparison with other measured clays standard, bentonite's fluorescence level was the weakest. Tab. 3 and 4 illustrate mean and median Raman intensity of β-carotene peak at 1512 cm^{-1} in the bentonite-gypsum mixture.

The decline in intensity remains noticeable but not as dramatic as with kaolinite. The rate of signal reduction is less sharp, showing a more gradual decrease. The most substantial impact occurs between 10 wt% and 30 wt% bentonite, with detectability greatly diminishing beyond this point, likewise it was with kaolin, indicating that even moderate amounts of clay can substantially interfere with signal detection. The minimal decrease between 30 and 50 wt% suggests that beyond a certain wt%, the addition of extra clay has a diminishing impact on further reducing the signal. Decrease between 50 and 70 wt% is relatively moderate compared to the first drop. Then reduction is more pronounced again,

between 70 and 90 wt% of bentonite. According to mean intensity values, at lower pigment concentrations (2.5 ppm and 1 ppm), the Raman signal becomes undetectable at higher bentonite contents (70 and 90 wt%).

Mixtures with bentonite display a more gradual decrease in intensity, with less severe interference, allowing detection of lower pigment concentrations compared to kaolinite. Even according to median data, which is normally worse comparing to mean, detection is still possible even for 50 clay wt% mixtures at 5 ppm of β-carotene. Weak spectral features are visible at 2.5 ppm concentration (Fig. 22).

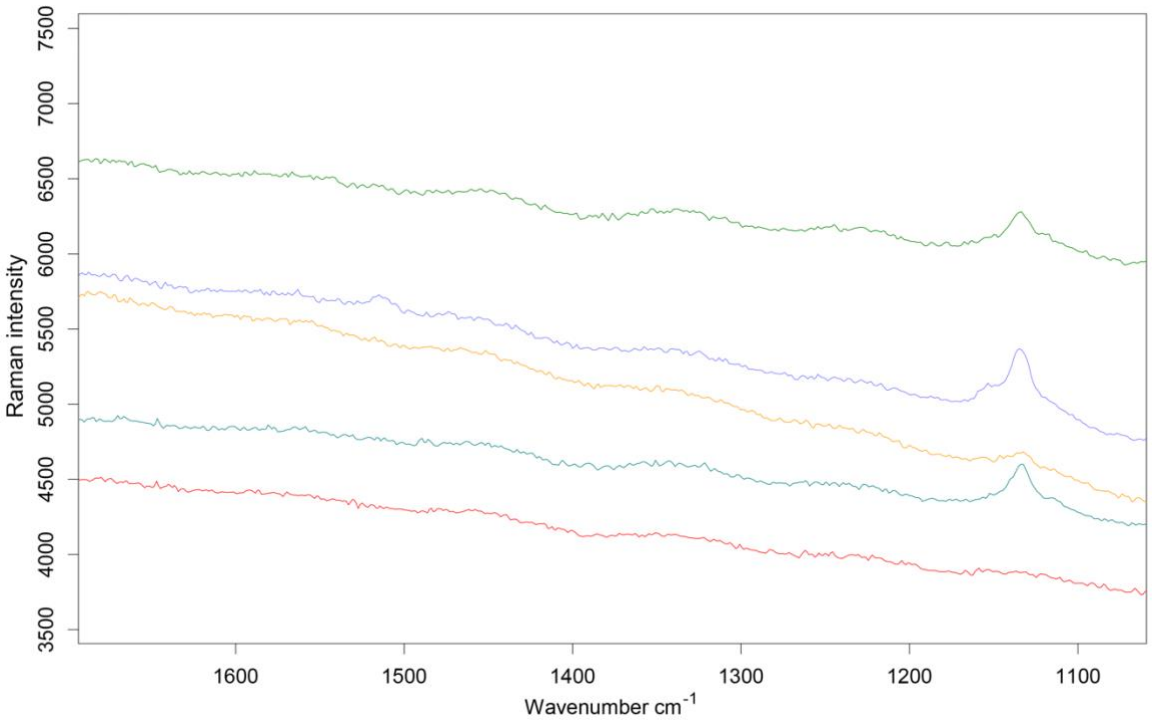

Fig. 22. Raman signal of β-carotene in the bentonite-gypsum mixture (2.5 ppm pigment concentration, blue: 10 wt%, turquoise: 30 wt%, green: 50 wt%, orange: 70 wt% and red: 90 wt% of bentonite GMZ)

	50 ppm	35 ppm	20 ppm	10 ppm	5 ppm	2.5 ppm	1 ppm
10 wt% of B	2188.1	748.7	538.4	254.4	139.6	16.4	7.9
30 wt% of B	1140.5	424.8	239.0	138.5	58.6	6.6	3.3
50 wt% of B	1011.6	386.8	231.8	136.2	53.2	6.5	3.0
70 wt% of B	692.2	315.6	210.7	103.1	33.3	0	0
90 wt% of B	594.6	300.6	194.8	83.2	27.1	0	0

Tab. 3. Mean Raman intensity of β-carotene peak at 1512 cm^{-1} in the bentonite-gypsum mixture

	50 ppm	35 ppm	20 ppm	10 ppm	5 ppm	2.5 ppm	1 ppm
10 wt% of B	2147.9	732.5	521.6	236.2	134.9	0	0
30 wt% of B	1181.1	414.2	227.1	138.5	64.0	0	0
50 wt% of B	937.4	402.4	216.0	122.3	63.0	0	0

70 wt% of B	675.4	303.8	208.4	97.0	0	0	0
90 wt% of B	595.1	287.7	183.9	91.2	0	0	0

Tab. 4. Median Raman intensity of β-carotene peak at 1512 cm^{-1} in the bentonite-gypsum mixture

Graphical demonstration of mean β-carotene Raman signal intensity is shown on Fig. 23. Respectively, data for median values is shown on Fig. 24.

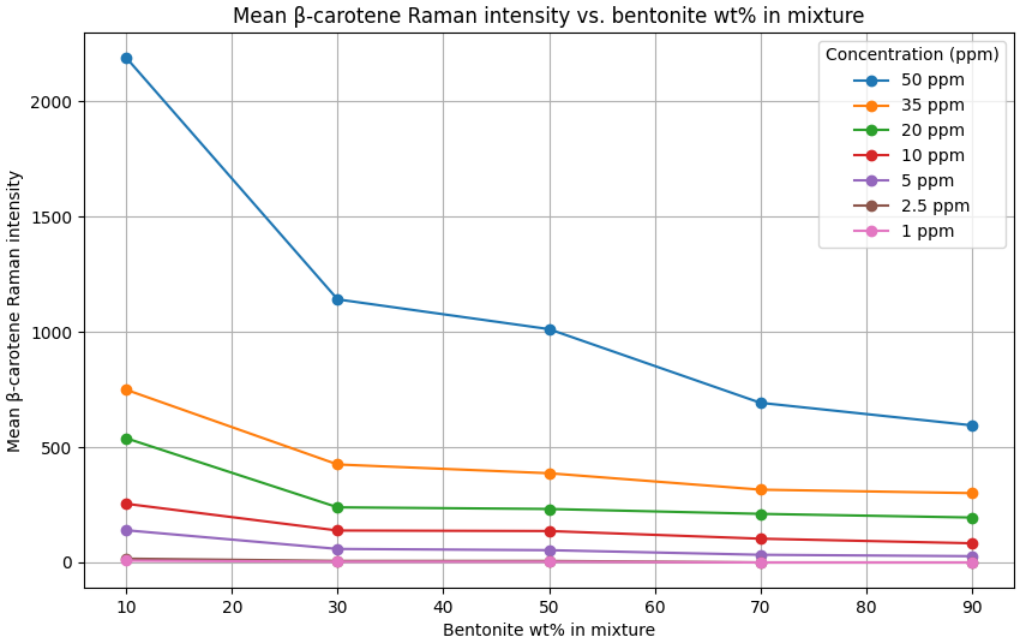

Fig. 23. Mean Raman intensity of β-carotene peak at 1512 cm^{-1} in the bentonite-gypsum mixture

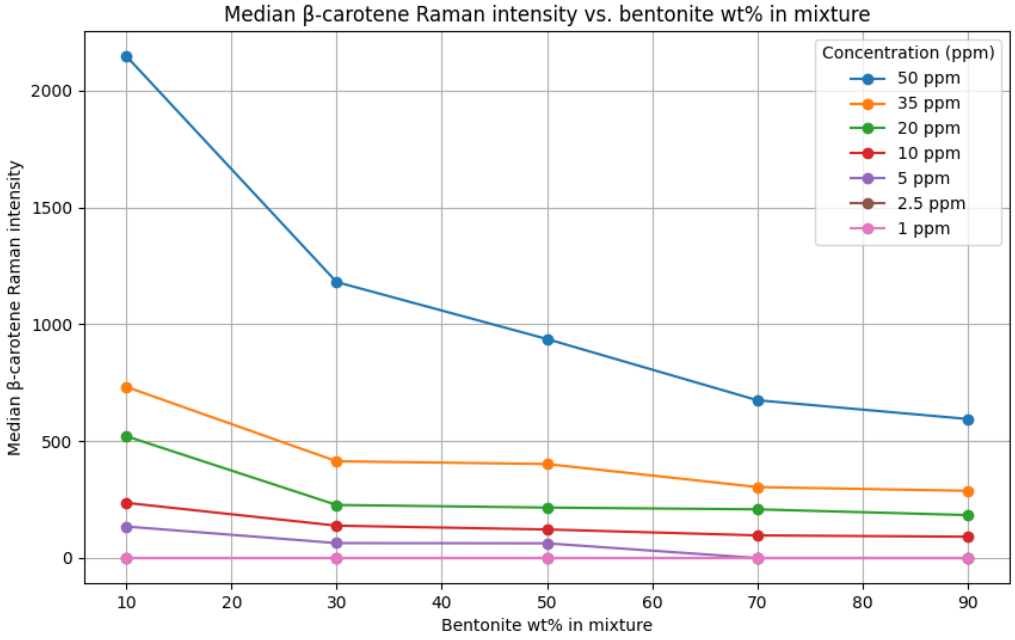

Fig. 24. Median Raman intensity of β-carotene peak at 1512 cm^{-1} in the bentonite-gypsum mixture

The approximation model suited for kaolin mixtures may not fit bentonite mixtures same well. Bentonite causes a more gradual and less severe decrease in signal intensity, making polynomial or power-law models more appropriate than exponential or hyperbolic. Quick signal drop of pigment in mixtures with kaolin aligns with models capturing sharp declines, while for mixtures with bentonite gradual decrease is better represented by models that account for smoother changes. Tab. 5 illustrates mean % decrease from 10 wt% of clay for 30, 50, 70 and 90 wt% mixtures. It's evident, that behavior on the first interval from 10 to 30 wt% is similar for both clays – mean drop by 51% for kaolin and 52.5% for bentonite mixtures. Therefore, it can be concluded that the signal deteriorates by approximately half over this interval.

Sedlec Ia Kaolin			**Bentonite GMZ**		
clay wt%	mean decrease from 10 wt% of clay	difference from previous value	clay wt%	mean decrease from 10 wt% of clay	difference from previous value
10			**10**		
30	-51%		**30**	-52.5%	
		-20.1%			-3.1%
50	-71.1%		**50**	-55.6%	
		-18.2%			-19.1%
70	-89.3%		**70**	-74.7%	
		-10.1%			-3%
90	-99.4%		**90**	-77.7%	

Tab. 5. Comparison of mean decrease from 10 wt% of selected clays for each next wt%. Source data: Mean Raman intensity of β-carotene peak at 1512 cm^{-1} in the kaolin-gypsum and bentonite-gypsum mixtures

5. Discussion

As it was already mentioned, Vítek et. al, 2009b conducted an experiment similar to ours, measuring the detectability of β-carotene in gypsum matrix at various pigment concentrations using a laboratory Raman spectrometer. In contrast, our study utilized a portable handheld Raman spectrometer, which is expected to have lower sensitivity. The difference in sensitivity between laboratory and handheld spectrometers is significant; the first ones typically offer higher resolution and better signal-to-noise ratios, which enhances their ability to detect lower concentrations of analytes. Thus, while similar research has been already conducted, the comparison of results can only be approximate due to differences in initial parameters and conditions. Factors such as the characteristics of the spectrometer, the excitation used, and the measurement of pure mixtures vs. ones with fluorescent component affect the comparability. Nevertheless, the detection limits of under 1 ppm β-carotene in gypsum matrix achieved in previous research might appear comparable to our results, where the pigment in gypsum-clay mixture was detectable at concentrations of 1 ppm and higher.

Relationship between spot size and detection sensitivity also should be taken into account. A larger spot size does indeed collect a greater amount of scattered light from a larger area of the sample, which can improve the overall signal intensity and potentially enhance the detection of low-concentration analytes. However, this can come at the cost of spatial resolution and specificity (Kneipp et. al., 1999).

In this thesis, we studied Raman signal intensity of β-carotene in mixtures with gypsum and selected clays across varying wt%. As anticipated, the fluorescence induced by the clay mineral led to a decrease in the pigment's signal intensity. However, our observations revealed a non-linear decline in signal intensity that necessitated a deeper analysis, non-linearity was observed both in kaolin and bentonite mixtures.

There are several possible causes of such behaviour and several phenomena that might explain such spectral patterns.

The interaction between β-carotene and the clay mineral can affect the Raman signal intensity:

Pigment can physically adsorb on the clay’s surface. This changes its molecular environment and, consequently, its spectral characteristics, including Raman signal intensity. With increasing clay mineral content, the surface area available for adsorption increases, but in a non-linear way, as different concentrations lead to different degrees of adsorption center saturation. Clay minerals may contain active sites such as metal ions or acidic groups that can interact directly with β-carotene. Such interactions can alter the structure of carotenoid, which is also reflected in its Raman signal.

Initially, as the concentration of the clay mineral increases from 10 to 30 wt%, fluorescence effects and adsorption sharply intensify, leading to a significant decrease in the Raman signal intensity. At concentrations from 30 to 50 wt%, adsorption center and fluorescence saturation may be observed, slowing the decrease. At concentrations above 50 wt%, more complex interactions between the components of the mixture might occur, such as particle aggregation, which can again slightly accelerate the signal drop.
Also, at high concentrations of the clay mineral, the optical properties of the mixture might change. The number of scattering and absorbing particles increases, affecting paths of the laser and the collected signal. These changes also can affect the intensity of background and Raman signals.

In the initial stages of increasing the concentration of the clay mineral (from 10 to 30 wt%), the number of fluorescent centers can significantly increase, leading to a substantial increase in background fluorescence and, consequently, a significant reduction in the Raman signal of β-carotene. As the clay mineral wt% further increases, the number of fluorescent centers may reach some saturation, meaning that adding more clay will not lead to the same significant increase in fluorescence. This possibly results in a slowing down of the decrease in Raman signal intensity.

For more detailed analysis, additional experiments should be conducted. And there are several ideas how experiment's design might be adavanced and impruved.

- Ensure more homogeneous mixing of the components using more advanced techniques. This will help achieve a more consistent distribution of particles.

- Use spectrofluorometry to measure the fluorescence intensity of the clay mineral at different concentrations. This will help quantify the contribution of fluorescence to the Raman signal reduction.

- Use Electron Microscopy techniques to analyze the morphology and distribution of the components in the mixture at different concentrations and explore interactions between β-carotene and clay minerals at the nanoscale.

- Investigate the effects of another types of clay minerals to see if the observed non-linear fluorescence effect is specific to the clay minerals used.

- Experiment with a larger data set and more detailed wt% segmentation. Also performing more replicates for each concentration will increase the reliability of the results. Statistical analysis will be more accurate.

Therefore, there are approaches to extend the existing data set and provide a more detailed explanation for the observed phenomena.

6. Conclusions

The primary aim of our experiment included studying the detection limits of possible biomarker using miniaturized handheld Raman spectrometer. We evaluated how presence of clay minerals, exhibiting fluorescence, can influence weaker Raman signals and affect performance of the miniaturized spectrometer. By analyzing gypsum mixed with selected clay minerals and β-carotene, which was chosen as model biomarker, our study reveals how different factors influence spectral patterns and interference, offering insights into the spectrometer's efficacy in detecting potential biosignatures amidst complex Martian mineralogy.

In mixtures of gypsum and Sedlec Ia kaolin, β-carotene spectral features were still detectable at 5 ppm with 10 wt% of kaolin based on mean values, while median data indicated a detection limit of 10 ppm for the same proportion. For kaolin concentrations between 30 and 50 wt%, the detection limit ranged from 10 to 20 ppm, with median values reaching zero at 10 ppm. At the highest kaolin concentration of 90 wt%, β-carotene was detectable only at the highest concentration of 50 ppm and was undetectable at 35 ppm.

In summary, detection limits were 5-10 ppm for 10 wt% kaolin, 10-20 ppm for 30-50 wt%, approximately 20-35 ppm for 70 wt%, and 50 ppm or higher for 90 wt% of kaolin in the mixture.

In mixtures of gypsum and bentonite GMZ, the detection limits for β-carotene were notably lower. In some cases, the pigment was detectable at concentrations as low as 2.5 and 1 ppm with 10, 30, and even 50 wt% of bentonite. At higher bentonite concentrations of 70-90 wt%, the pigment was detectable at concentrations closer to 10 ppm.

Overall, the detection limits for β-carotene in gypsum-bentonite mixture were 1-5 ppm for 10-50 wt% of bentonite, and 5-10 ppm for 70-90 wt% bentonite.

A common observation in both mixtures was a sharp decline in signal intensity during the initial stage between 10 and 30 wt%.

In the mixture with Sedlec Ia kaolin, which exhibited much stronger fluorescence, the β-carotene signal decline was sharper. In contrast, the decline in signal intensity in the mixture with bentonite GMZ, which fluoresced less intensely, displayed a more stepwise pattern.

In conclusion, the detection limits of β-carotene in mixtures with the studied clay minerals, are in average the lower tens of ppm. These results are first of all relevant to the miniaturized Raman spectrometer used in this study.

References

APXS Composition Results". *NASA*. https://web.archive.org/web/20160603120939/http://nssdc.gsfc.nasa.gov/planetary/marspath/apxs.html (22.07.2024)

Basics of Raman spectroscopy: Anton Paar Wiki. 2024. https://wiki.anton-paar.com/en/basics-of-raman-spectroscopy/ (22.07.2024)

BERGAYA, F.; LAGALY, G. General introduction: clays, clay minerals, and clay science. *Developments in Clay Science*, 2006, 1: 1-18.

BHARTIA, R., et al. Perseverance's scanning habitable environments with Raman and luminescence for organics and chemicals (SHERLOC) investigation. *Space Science Reviews*, 2021, 217: 58.

BIBRING, J-P., et al. Mars surface diversity as revealed by the OMEGA/Mars Express observations. *Science*, 2005, 307: 1576-1581.

BIBRING, J-P., et al. Global mineralogical and aqueous Mars history derived from OMEGA/Mars Express data. *Science*, 2006, 312: 400-404.

BISHOP, J. L., et al. Phyllosilicate diversity and past aqueous activity revealed at Mawrth Vallis, Mars. *Science*, 2008, 321: 830-833.

BISHOP, J. L.; RAMPE, E. B. Evidence for a changing Martian climate from the mineralogy at Mawrth Vallis. *Earth and Planetary Science Letters*, 2016, 448: 42-48.

BROCKS, J. J. Biomarkers (molecular fossils). *Encyclopaedia of Biogeology*, 2011, 147-167.

CHEN, Y., et al. Ancient microorganisms and carotenoids preserved in fluid inclusions in halite from Chaka Salt Lake, Western China: Evidence from micro-observation and in situ Raman Spectroscopy. *Acta Geologica Sinica-English Edition*, 2021, 95: 1008-1015.

CHRISTENSEN, P. R., et al. Detection of crystalline hematite mineralization on Mars by the Thermal Emission Spectrometer: Evidence for near-surface water. *Journal of Geophysical Research: Planets*, 2000, 105: 9623-9642.

CLARK, B. C.; BAIRD, A. K. Is the Martian lithosphere sulfur rich? *Journal of Geophysical Research: Solid Earth*, 1979, 84: 8395-8403.

CLARK, B. C., et al. Chemical composition of Martian fines. *Journal of Geophysical Research: Solid Earth*, 1982, 87: 10059-10067.

CLOUTIS, E., et al. Identification and discrimination of polycyclic aromatic hydrocarbons using Raman spectroscopy. *Icarus*, 2016, 274: 211-230.

COCKELL, C. S.; KNOWLAND, J. Ultraviolet radiation screening compounds. *Biological Reviews*, 1999, 74: 311-345.

COPELAND, B. J. Environmental characteristics of hypersaline lagoons. *Publications of the Institute for Marine Science (University of Texas)*, 1967, 12: 207-218.

CRISLER, J. D., et al. Bacterial growth at the high concentrations of magnesium sulfate found in Martian soils. *Astrobiology*, 2012, 12: 98-106.

CRONIN, J. R.; COOPER, G. W.; PIZZARELLO, S. Characteristics and formation of amino acids and hydroxy acids of the Murchison meteorite. *Advances in Space Research*, 1995, 15: 91-97.

ECKHARDT, G., et al. Stimulated Raman scattering from organic liquids. *Physical Review Letters*, 1962, 9: 455.

EHLMANN, B. L., et al. Identification of hydrated silicate minerals on Mars using MRO-CRISM: Geologic context near Nili Fossae and implications for aqueous alteration. *Journal of Geophysical Research: Planets*, 2009, 114.

EHLMANN, B. L.; EDWARDS, C. S. Mineralogy of the Martian surface. *Annual Review of Earth and Planetary Sciences*, 2014, 42: 291-315.

Encyclopaedia Britannica. Clay mineral.
https://www.britannica.com/science/clay-mineral (22.07.2024)

FARRAND, W. H., et al. VNIR multispectral observations of rocks at Cape York, Endeavour crater, Mars by the Opportunity rover's Pancam. *Icarus*, 2013, 225: 709-725.

FOUCHER, F., et al. Definition and use of functional analogues in planetary exploration. *Planetary and Space Science*, 2021, 197: 105162.

GAINEY, S. R.; HAUSRATH, E. M.; HUROWITZ, J. A. Thermodynamic and kinetic analysis of transitions in clay mineral chemistry on Mars. *Icarus*, 2022, 372: 114733.

GARCIA-PICHEL, F.; CASTENHOLZ, R. W. Occurrence of UV-absorbing, mycosporine-like compounds among cyanobacterial isolates and an estimate of their screening capacity. *Applied and Environmental Microbiology*, 1993, 59: 163-169.

GATES, W., et al. *Infrared and Raman spectroscopies of clay minerals*. Elsevier, 2017.

GENDRIN, A., et al. Sulphates in Martian layered terrains: the OMEGA/Mars Express view. *Science*, 2005, 307: 1587-1591.

GIANI, M.; MARTÍNEZ-ESPINOSA, R. M. Carotenoids as a protection mechanism against oxidative stress in Haloferax mediterranei. *Antioxidants,* 2020, 9: 1060.

GLAVIN, D. P., et al. Evidence for perchlorates and the origin of chlorinated hydrocarbons detected by SAM at the Rocknest aeolian deposit in Gale Crater. *Journal of Geophysical Research: Planets*, 2013, 118: 1955-1973.

GUGGENHEIM, S., et al. Introduction to the properties of clay minerals. *Teaching Mineralogy (Eds: Brady, J. B, DW Mogk, D. Perkins). Mineralogical Society of America. Washington, DC*, 1997, 371-388.

GUNDE-CIMERMAN, N.; PLEMENITAŠ, A.; OREN, A.. Strategies of adaptation of microorganisms of the three domains of life to high salt concentrations. *FEMS Microbiology Reviews*, 2018, 42: 353-375.

HARVEY, D.. Analytical Chemistry 2.0 — an open-access digital textbook. *Analytical and Bioanalytical Chemistry*, 2011, 399: 149-152.

HASKIN, L. A., et al. Water alteration of rocks and soils on Mars at the Spirit rover site in Gusev crater. *Nature*, 2005, 436: 66-69.

HAZEN, R. M., et al. Clay mineral evolution. *American Mineralogist*, 2013, 98: 2007-2029.

HOLLIS, J. R., et al. A deep-ultraviolet Raman and fluorescence spectral library of 62 minerals for the SHERLOC instrument onboard Mars 2020. *Planetary and Space Science*, 2021, 209: 105356.

HOSSAIN, M. N., et al. Influence of moisture variation on the performance of Raman spectroscopy in quantitative pharmaceutical analyses. *Journal of pharmaceutical and biomedical analysis*, 2019, 164: 528-535.

HUGGETT, J. M. Clay minerals. *Encyclopedia of Geology*. 2013, 10.

KNEIPP, K., et al. Ultrasensitive chemical analysis by Raman spectroscopy. *Chemical Reviews*, 1999, 99: 2957-2976.

KOCHHAR, N., et al. Perspectives on the microorganism of extreme environments and their applications. *Current Research in Microbial Sciences*, 2022, 3: 100134.

KUMARI, N.; MOHAN, C. Basics of clay minerals and their characteristic properties. *Clays and Clay Minerals*, 2021, 24: 1-29.

LONG, D. A. Raman spectroscopy. *New York*, 1977, 1: 310.

LONG, D. A. Early history of the Raman effect. *International Reviews in Physical Chemistry*, 1988, 7: 317-349.

MALENFANT, J., et al. Towards routine organic structure determination using Raman microscopy. *Chemical Science*, 2024, 15: 701-709.

MARSHALL, C. P., et al. Carotenoid analysis of halophilic Archaea by resonance Raman spectroscopy. *Astrobiology*, 2007, 7: 631-643.

MATIJEVIC, J. Sojourner: The Mars Pathfinder microrover flight experiment. *Space Technology*, 1997, 3: 143-149.

MCCREERY, R. L. *Raman spectroscopy for chemical analysis*. John Wiley & Sons, 2005.

MILLAN, M., et al. Influence of calcium perchlorate on organics under SAM-like pyrolysis conditions: Constraints on the nature of Martian organics. *Journal of Geophysical Research: Planets*, 2020.

MURCHIE, S. L., et al. A synthesis of Martian aqueous mineralogy after 1 Mars year of observations from the Mars Reconnaissance Orbiter. *Journal of Geophysical Research: Planets*, 2009.

MUSTARD, J. M., et al. Hydrated silicate minerals on Mars observed by the CRISM instrument on Mars Reconnaissance Orbiter. *Nature*, 2008, 354: 305-309.

NOE DOBREA, E. Z., et al. Spectral and geomorphic evidence for a past inland sea in Eridania basin, Mars. In: *AGU Fall Meeting Abstracts*. 2008. p. P32B-03.

OREN, A.; KÜHL, M.; KARSTEN, U. An endoevaporitic microbial mat within a gypsum crust: zonation of phototrophs, photopigments, and light penetration. *Marine Ecology Progress Series*, 1995, 128: 151-159.

OREN, A. Bioenergetic aspects of halophilism. *Microbiology and Molecular Biology Reviews*, 1999, 63: 334-348.

PAVÓN, E.; ALBA, M. D. Swelling layered minerals applications: A solid state NMR overview. *Progress in Nuclear Magnetic Resonance Spectroscopy*, 2021, 124: 99-128.

PHUA, Y. Y., et al. Characterizing hydrated sulfates and altered phases in Jezero Crater fan and floor geologic units with SHERLOC on Mars 2020. *Journal of Geophysical Research: Planets*, 2024, 129: e2023JE008251.

PONTEFRACT, A., et al. Microbial diversity in a hypersaline sulfate lake: a terrestrial analog of ancient Mars. *Frontiers in Microbiology*, 2017, 8: 1819.

POULET, F., et al. Phyllosilicates on Mars and implications for early Martian climate. *Nature*, 2005, 438: 623-627.

POURKARIMI, S., et al. Factors affecting production of beta-carotene from Dunaliella salina microalgae. *Biocatalysis and Agricultural Biotechnology*, 2020, 29: 101771.

PRIETO-BARAJAS, C. M.; VALENCIA-CANTERO, E.; SANTOYO, G. Microbial mat ecosystems: structure types, functional diversity, and biotechnological application. *Electronic Journal of Biotechnology*, 2018, 31: 48-56.

QUINN, D. P.; EHLMANN, B. L. The deposition and alteration history of the northeast Syrtis Major layered sulphates. *Journal of Geophysical Research: Planets*, 2019, 124: 1743-1782.

RIEDER, R., et al. The chemical composition of Martian soil and rocks returned by the mobile alpha proton X-ray spectrometer: Preliminary results from the X-ray mode. *Science*, 1997, 278: 1771-1774.

ROTHSCHILD, L. J. Earth analogs for Martian life. Microbes in evaporites, a new model system for life on Mars. *Icarus*, 1990, 88: 246-260.

SCHRADER, B. (ed.). *Infrared and Raman spectroscopy: methods and applications*. John Wiley & Sons, 2008.

SCHUBERT, B. A., et al. Dunaliella cells in fluid inclusions in halite: significance for long-term survival of prokaryotes. *Geomicrobiology Journal*, 2010, 27: 61-75.

SEDLÁČKOVÁ, M. Hydromechanické charakteristiky kaolinových suspensí. Přírodovědecká fakulta, Univerzita Karlova, 2019.

SQUYRES, S. W., et al. The opportunity rover's Athena science investigation at Meridiani Planum, Mars. *Science*, 2004, 306: 1698-1703.

STIVALETTA, N., et al. Endolithic microorganisms from mound evaporite deposits (Southern Tunisia). *Origins of Life and Evolution of the Biosphere*, 2010, 40: 536-537.

ŠEBEK, J., et al. Spectroscopy of the C–H stretching vibrational Band in selected Organic molecules. *The Journal of Physical Chemistry A*, 2013, 117: 7442-7452.

TOSCA, N. J., et al. Geochemical modeling of evaporation processes on Mars: Insight from the sedimentary record at Meridiani Planum. *Earth and Planetary Science Letters*, 2005, 240: 122-148.

VANIMAN, D. T., et al. Mineralogy of a mudstone at Yellowknife Bay, Gale crater, Mars. *Science*, 2014, 343: 1243480.

VÍTEK, P., et al. Beta-carotene — a possible biomarker in the Martian evaporitic environment: Raman micro-spectroscopic study. *Planetary and Space Science*, 2009a, 57: 454-459.

VÍTEK P., et al. Identification of β-carotene in an evaporitic matrix — evaluation of Raman spectroscopic analysis for astrobiological research on Mars. *Analytical and Bioanalytical chemistry*, 2009b, 393: 1967-1975.

VÍTEK, P. Identification of microbial pigments in evaporites using Raman spectroscopy: implications for astrobiology. Přírodovědecká fakulta, Univerzita Karlova, 2010.

WANG, A., et al. Sulfate deposition in subsurface regolith in Gusev crater, Mars. *Journal of Geophysical Research: Planets*, 2006, 111.E2.

WARREN, J. K. *Evaporites: sediments, resources and hydrocarbons*. Springer Science & Business Media, 2006.

WEI, D.; CHEN, S.; LIU, Q. Review of fluorescence suppression techniques in Raman spectroscopy. *Applied Spectroscopy Reviews*, 2015, 50: 387-406.

WIERZCHOS, J.; ASCASO, C.; MCKAY, C. P. Endolithic cyanobacteria in halite rocks from the hyperarid core of the Atacama Desert. *Astrobiology*, 2006, 6: 415-422.

WINTERS, Y. D.; LOWENSTEIN, T. K.; TIMOFEEFF, M. N. Identification of carotenoids in ancient salt from Death Valley, Saline Valley, and Searles Lake, California, using laser Raman spectroscopy. *Astrobiology*, 2013, 13: 1065-1080.

WRAY, J. J., et al. Phyllosilicates and sulphates at Endeavour crater, Meridiani Planum, Mars. *Geophysical Research Letters*, 2009, 36.

XI, Y., et al. β-Carotene production from Dunaliella salina cultivated with bicarbonate as carbon source. *Journal of Microbiology and Biotechnology*, 2020, 30: 868.

ZENOBI, R., et al. Spatially resolved organic analysis of the Allende meteorite. *Science*, 1989, 246: 1026-1029.

ZHANG, Y., et al. Montmorillonite alteration and its influence on Sr (II) adsorption on GMZ bentonite. *Environmental Earth Sciences*, 2021, 80: 1-12.

ZHANG, S. L., et al. Fourier transform Raman spectroscopy of fuels: curve-fitting of C-H stretching bands. *Spectrochimica Acta Part A: Molecular and Biomolecular Spectroscopy*, 1996, 52: 1529-1540.

БЕНУЭЛЛ, Колин. Основы молекулярной спектроскопии. *Мир*, 1985.

Appendices

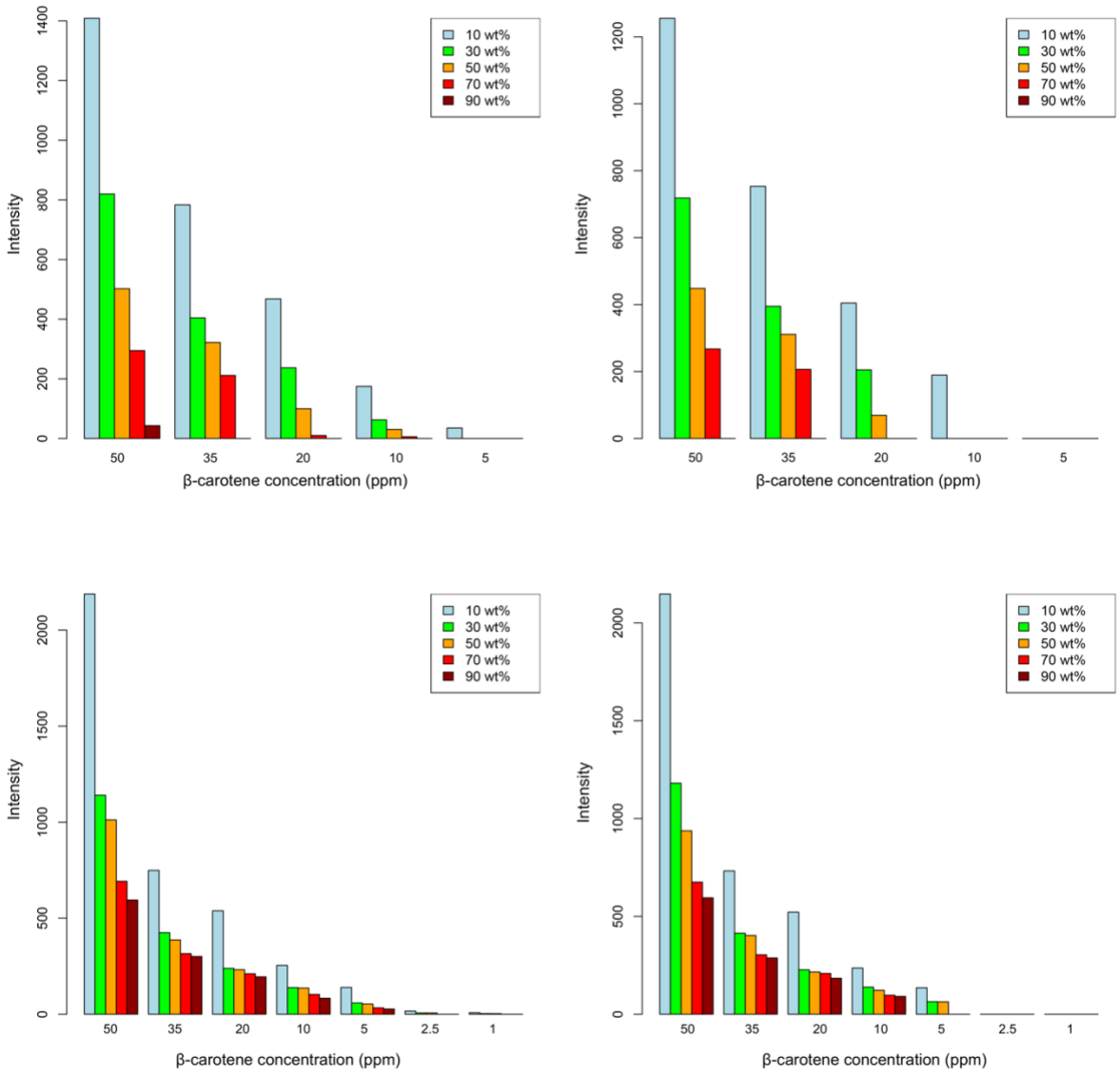

Fig. S1. β-carotene intensity decrease in various clay wt% mixtures at various pigment concentrations (top left: mean intensities in Sedlec kaolin mixture, top right: median intensities in Sedlec kaolin mixture, bottom left: mean intensities in bentonite GMZ, bottom right: median intensities in bentonite GMZ)

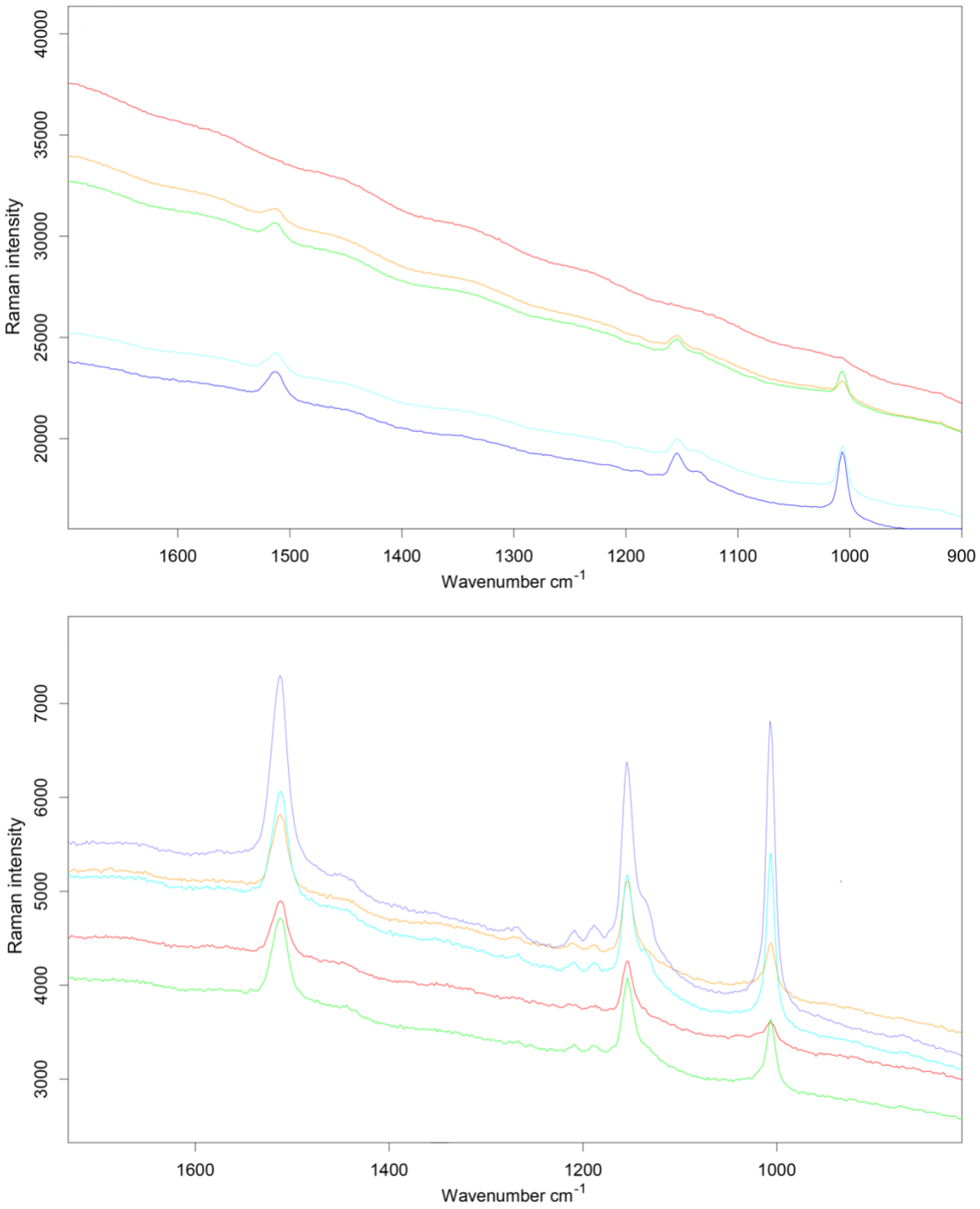

Fig. S2. Raman spectra of β-carotene in mixtures with kaolin (top) and bentonite (bottom) at 50 ppm concentration level. Blue: 10 wt% of clay, turquoise: 30 wt%, green: 50 wt%, orange: 70 wt% and red: 90 wt%.

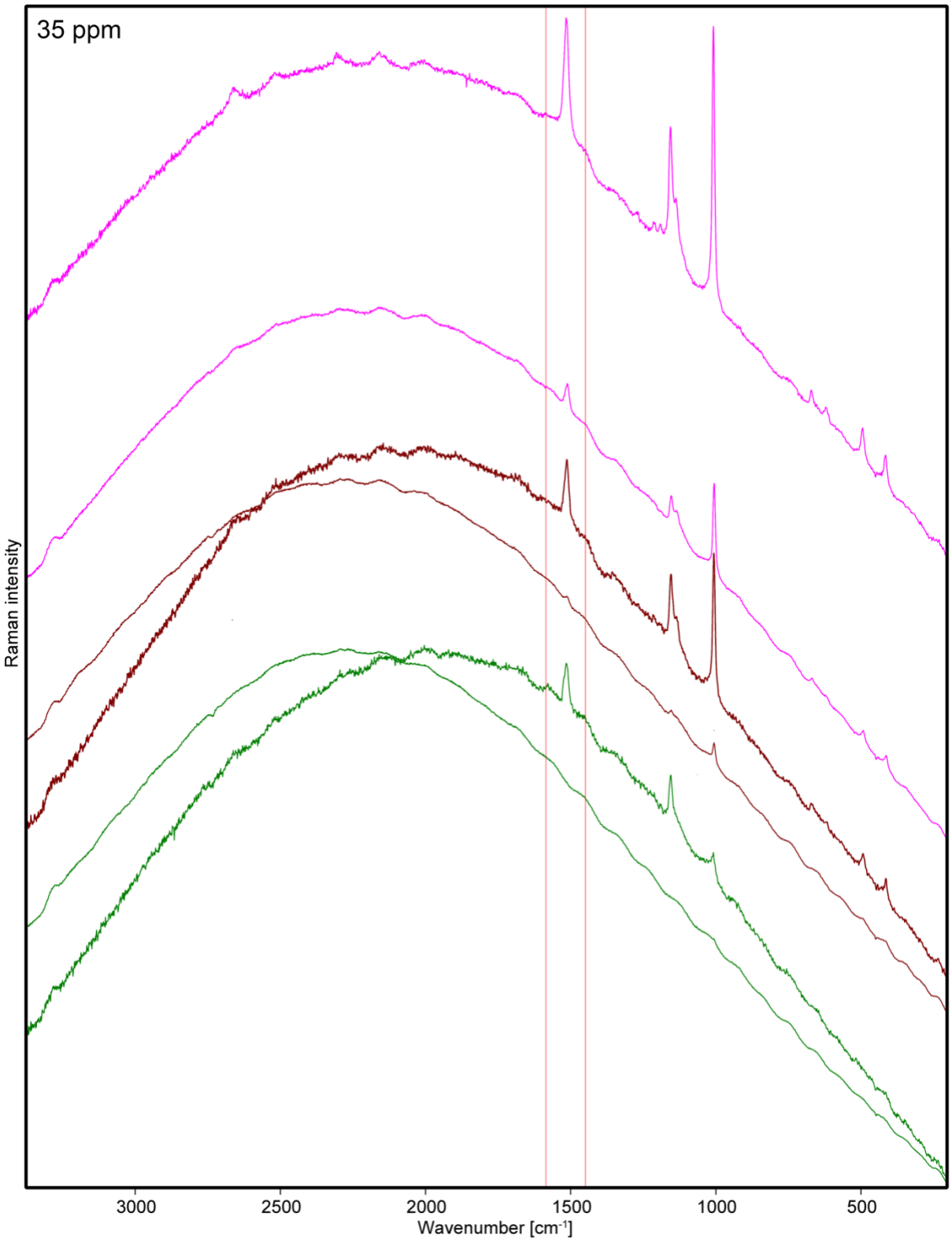

Fig. S3. Comparison of Raman spectra of β-carotene in mixtures with kaolin and bentonite at 35 ppm concentration level (from top to bottom: 10 wt% of bentonite, 10 wt% of kaolin, 50 wt% of bentonite, 50 wt% of kaolin, 90 wt% of bentonite, 90 wt% of kaolin)

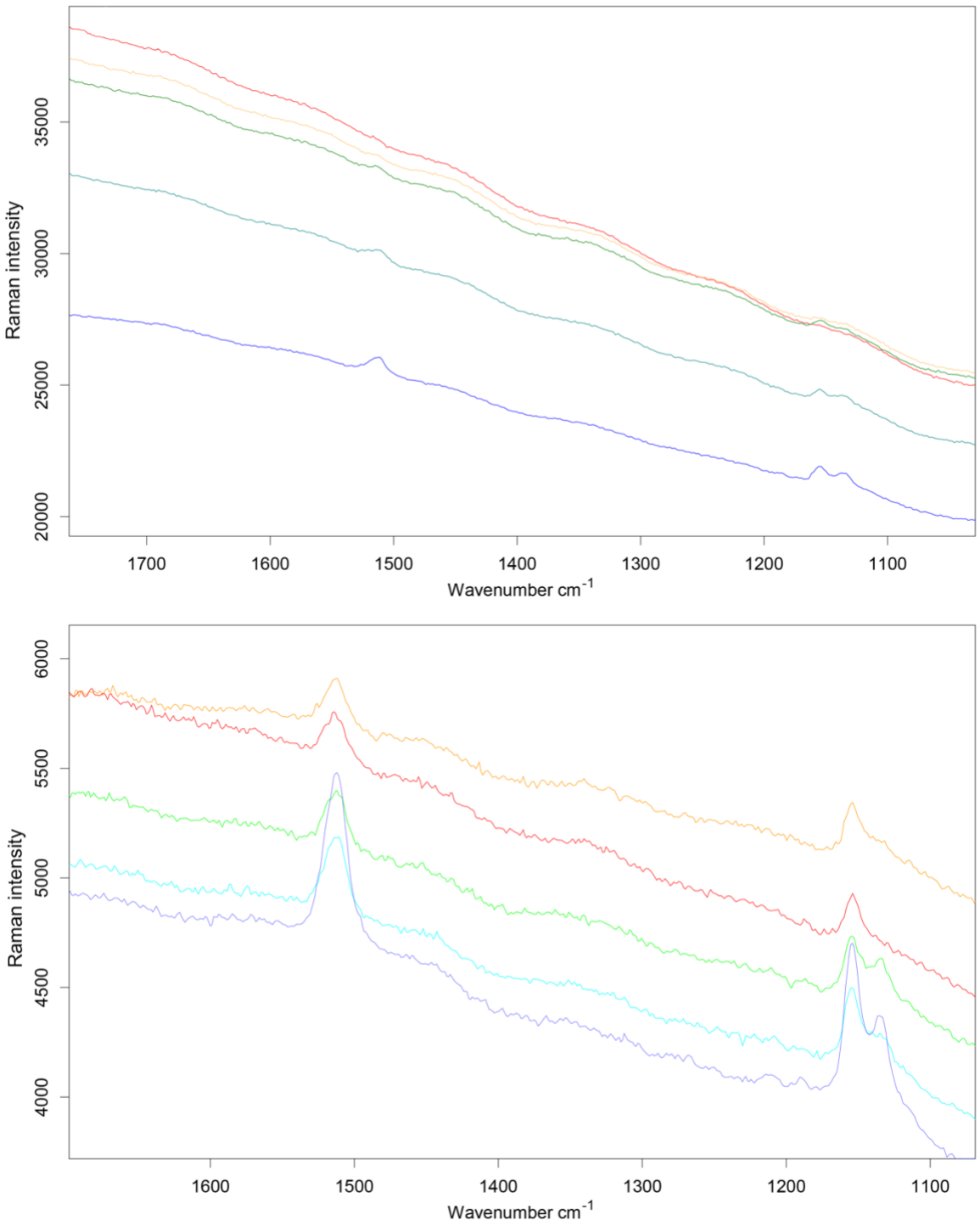

Fig. S4. Raman spectra of β-carotene in mixtures with kaolin (top) and bentonite (bottom) at 20 ppm concentration level. Blue: 10 wt% of clay, turquoise: 30 wt%, green: 50 wt%, orange: 70 wt% and red: 90 wt%.

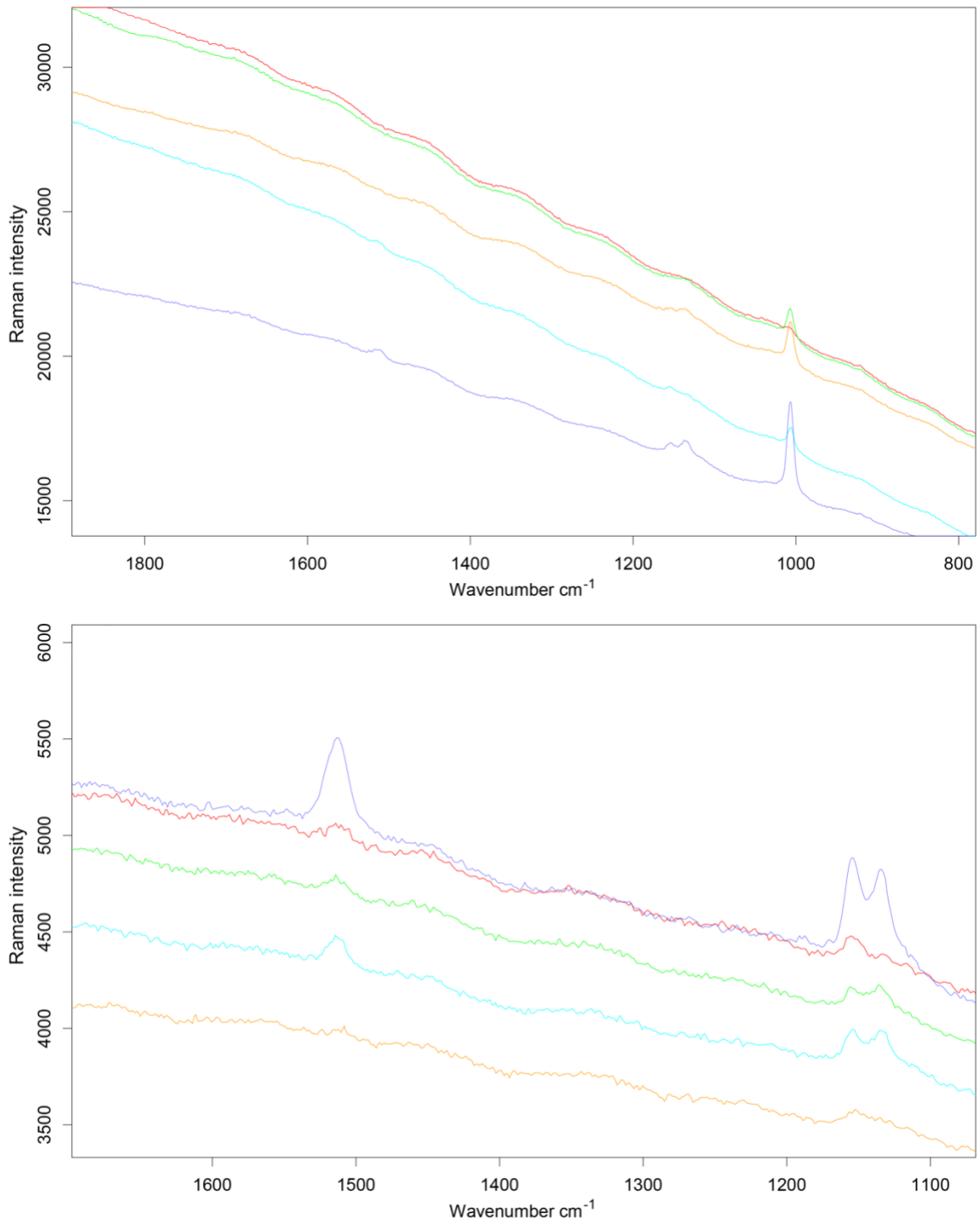

Fig. S5. Raman spectra of β-carotene in mixtures with kaolin (top) and bentonite (bottom) at 10 ppm concentration level. Blue: 10 wt% of clay, turquoise: 30 wt%, green: 50 wt%, orange: 70 wt% and red: 90 wt%.

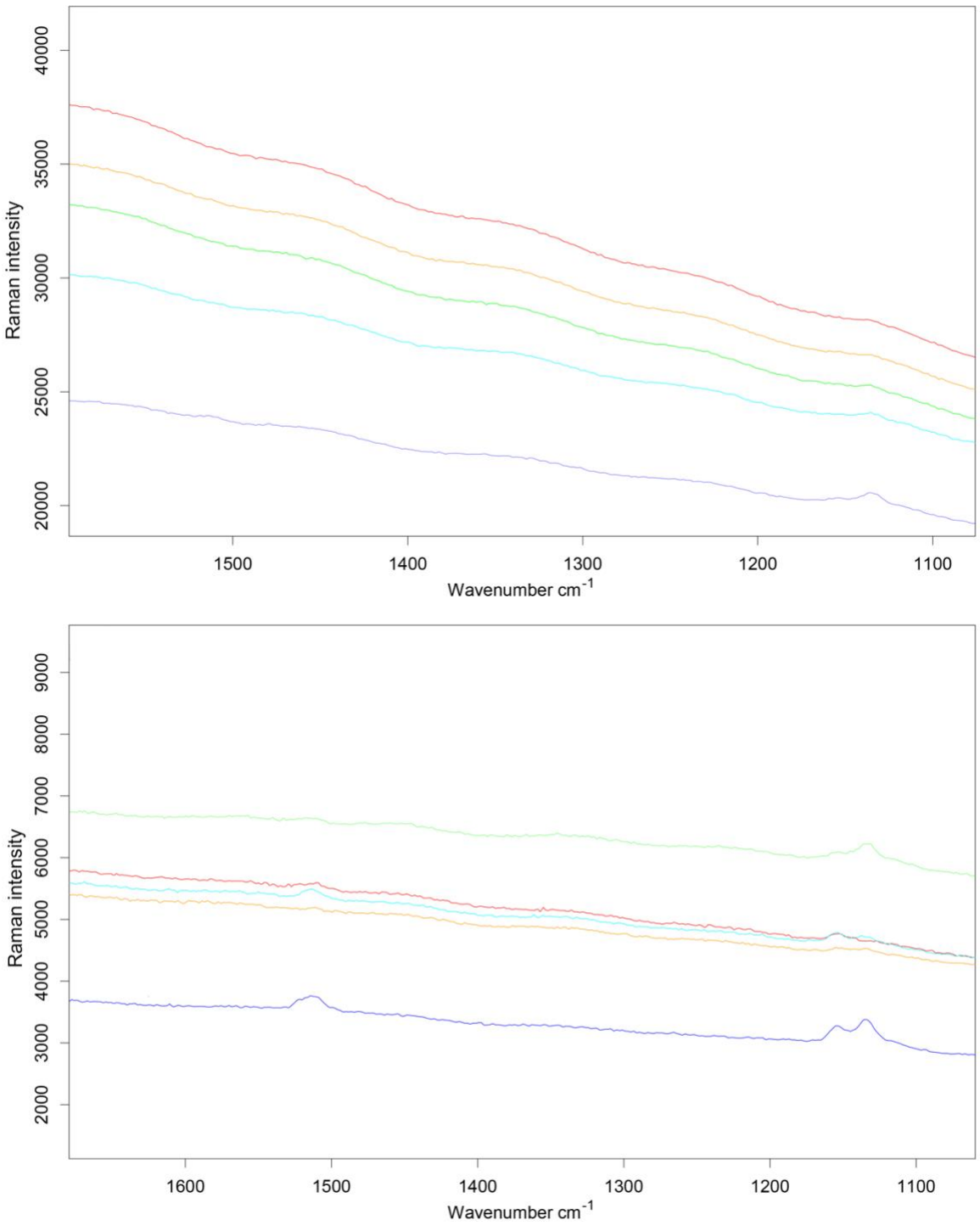

Fig. S6. Raman spectra of β-carotene in mixtures with kaolin (top) and bentonite (bottom) at 5 ppm concentration level. Blue: 10 wt% of clay, turquoise: 30 wt%, green: 50 wt%, orange: 70 wt% and red: 90 wt%.